

2 **Deglacial changes in flow and frontal structure through the Drake Passage**

3 **Authors:** J. Roberts<sup>1,2\*</sup>, I.N.McCave<sup>1</sup>, E.L. McClymont<sup>3</sup>, S. Kender<sup>4,5</sup>, C.-D. Hillenbrand<sup>2</sup>, R. Matano<sup>6</sup>,  
4 D.A. Hodell<sup>1</sup>, V.L. Peck<sup>2</sup>

5 **Affiliations:** <sup>1</sup> Godwin Laboratory for Palaeoclimate Research, Department of Earth Sciences,  
6 University of Cambridge, Downing Street, Cambridge, CB2 3EQ; <sup>2</sup> British Antarctic Survey, High Cross,  
7 Madingley Road, Cambridge, CB3 0ET; <sup>3</sup> Department of Geography, Durham University, South Road,  
8 Durham, DH1 3LE; <sup>4</sup> Camborne School of Mines, University of Exeter, Penryn Campus, Penryn,  
9 Cornwall TR10 9FE UK; <sup>5</sup> British Geological Survey, Nicker Hill, Keyworth, Nottingham, NG12 5GG; <sup>6</sup>  
10 College of Oceanic and Atmospheric Sciences, Oregon State University, Corvallis, Oregon, USA;

11 \*Now based at the Alfred-Wegener-Institut, Helmholtz-Zentrum für Polar- und Meeresforschung,  
12 Am Alten Hafen 26, 27568 Bremerhaven

13 **Correspondence to:** jenny.roberts@awi.de

14 **Keywords:** Cold Water Route; Sortable Silt; Deglacial; Alkenones; Sub-Antarctic Front

15 **Abstract:** The oceanic gateways of the Drake Passage and the Agulhas Current are critical locations  
16 for the inflow of intermediate-depth water masses to the Atlantic, which contribute to the shallow  
17 return flow that balances the export of deep water from the North Atlantic. The thermohaline  
18 properties of northward flowing intermediate water are ultimately determined by the inflow of  
19 water through oceanic gateways. Here, we focus on the less well-studied “Cold Water Route”  
20 through the Drake Passage. We present millennially-resolved bottom current flow speed and sea  
21 surface temperature records downstream of the Drake Passage spanning the last 25,000 years. We  
22 find that prior to 15 ka, bottom current flow speeds at sites in the Drake Passage region were  
23 dissimilar and there was a marked anti-phasing between sea surface temperatures at sites upstream  
24 and downstream of the Drake Passage. After 14 ka, we observe a remarkable convergence of flow  
25 speeds coupled with a sea surface temperature phase change at sites upstream and downstream of  
26 Drake Passage. We interpret this convergence as evidence for a significant southward shift of the  
27 sub-Antarctic Front from a position north of Drake Passage. This southward shift increased the  
28 through-flow of water from the Pacific, likely reducing the density of Atlantic Intermediate Water.  
29 The timing of the southward shift in the sub-Antarctic Front is synchronous with a major re-  
30 invigoration of Atlantic Meridional Overturning Circulation, with which, we argue, it may be linked.

## 31 Introduction

32 The export of North Atlantic Deep Water (NADW) to the South Atlantic requires a compensating  
33 intermediate-depth northward flow. Volume transport estimates suggest that Antarctic  
34 Intermediate Water (AAIW) is the main component of this upper layer return flow (Poole and  
35 Tomczak, 1999). Thermocline waters contributing to Atlantic AAIW enter the Atlantic either through  
36 Drake Passage (the Cold Water Route) or via the Agulhas Current (the Warm Water Route) (Poole  
37 and Tomczak, 1999). The water mass properties of these AAIW contributions are markedly different,  
38 with relatively cold-fresh water entering the southwest Atlantic via the Cold Water Route and  
39 warmer-saltier thermocline waters entering the southeast Atlantic via the Warm Water Route  
40 (Gordon et al., 1992). The relative contribution and thermohaline properties of these water masses  
41 determine the Atlantic's meridional heat and freshwater fluxes, and thus have implications for global  
42 climate.

43 Whilst there have been a large number of studies that have focused on the changes in the flow and  
44 thermohaline properties of water masses entering the southeast Atlantic via the Warm Water  
45 Route, there are relatively few proxy reconstructions of past changes in Cold Water Route inflow.

46 The inflow of water via the Cold Water Route is strongly influenced by the position of the oceanic  
47 fronts within the Drake Passage. Low-density Sub-Antarctic Mode Water (SAMW), formed in the  
48 southeast Pacific, is transported into the Atlantic basin north of the sub-Antarctic Front (SAF, the  
49 most northerly jet of the Antarctic Circumpolar Current, ACC) (Talley, 1999). Along its flow path  
50 through the Drake Passage, SAMW mixes with Antarctic-derived waters to ultimately form the cold-  
51 fresh AAIW end-member in the Atlantic. Determining the position of the SAF is therefore critical for  
52 understanding changes in the inflow of low-density intermediate water via the Cold Water Route in  
53 the past.

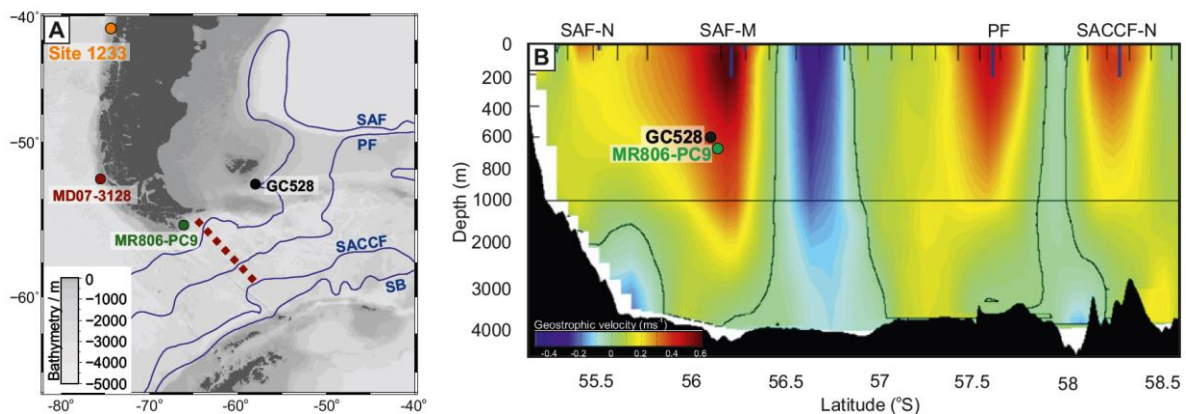
54 Sea surface temperature (SST)-based reconstructions of the SAF during the last glacial period suggest  
55 that it was 5-10° northwards of its present position (e.g. Gersonde et al., 2005); however,  
56 reconstructions of the position of the SAF in the Drake Passage region remain scarce. Estimates of  
57 bottom current speed (McCave et al., 1995) provide a more direct means to determine relative  
58 changes in Cold Water Route through-flow. To-date, the only two flow speed reconstructions from  
59 within (Lamy et al., 2015) and downstream (McCave et al., 2014) of the Drake Passage are relatively  
60 low resolution across the last deglaciation and their interpretation of deglacial changes in flow via  
61 the Cold Water Route are contradictory.

62 Here, we use a multi-proxy approach to determine changes in the structure and flow of water  
63 through the Cold Water Route over the last deglaciation. We present sub-millennially-resolved  
64 bottom current flow speed and alkenone-based SST reconstructions from a site immediately  
65 downstream of Drake Passage spanning the last 25 kyr. Comparison with other SST and bottom  
66 current flow speed records from the Drake Passage region reveals that the Last Glacial Maximum  
67 (LGM) and early deglacial was characterised by a very different spatial pattern of SSTs and bottom  
68 current flow speeds relative to the last 14 kyr, suggesting Cold Water Route through-flow during the  
69 glacial period was reduced.

## 70 2. Materials and Methods

### 71 2.1 Core Material

72 This study is based on the sediment core GC528 (53°0.8'S, 58°2.4'W, 598 m) located on the southern  
73 flank of the Falkland Plateau collected on the cruise JR244 of the RRS *James Clark Ross*. The core was  
74 taken from a contourite drift (South Falkland Slope Drift; Koenitz et al., 2008), that is today located  
75 under the core of a strong westerly jet associated with the SAF (Figure 1) and is bathed by AAIW.



76  
77 *Figure 1: (A) Bathymetric map of Drake Passage showing the annual mean position of the*  
78 *circumpolar fronts in blue (from N to S: SAF = Sub-Antarctic Front; PF = Polar Front; SACCF = Southern*  
79 *Antarctic Circumpolar Current Front; SB = Southern Boundary of the ACC) (Orsi et al., 1995), core sites*  
80 *and location of flow speed profile shown in Fig. 1B (dotted red line); (B) Geostrophic flow velocities on*  
81 *transect through Drake Passage (Renault et al., 2011). Core positions have been projected onto this*  
82 *transect.*

83 The top 50cm of GC528 (Holocene sediments) consist of foraminifera ooze containing >10% CaCO<sub>3</sub>  
84 and alkenone concentrations of >1 µg/g. The rest of the sequence is mainly composed of silt-bearing  
85 clay with occasional dropstones present (particularly towards the LGM). Weight percent carbonate is  
86 ~1% and the alkenone concentration is 0.5-1 µg/g.

87 The age model for core GC528 is based on reservoir-age corrected AMS  $^{14}\text{C}$  dates on monospecific  
88 benthic foraminifera and has been described in full in Roberts et al. (2016). The sedimentation rate  
89 varies from 7 cm/kyr in the Holocene to 50 cm/kyr during the glacial.

## 90 2.2 Methods

### 91 2.2.1 Sortable silt grain size analysis

92 Sediment grain size distribution in the silt fraction (10-63  $\mu\text{m}$ ) is strongly controlled by the  
93 geostrophic speed occurring above the bottom mixed layer (McCave et al., 1995). A detailed grain  
94 size analysis of the silt fraction (with an average temporal resolution of 200 years), in which  
95 carbonate and biogenic silica had been removed (McCave et al., 1995), was performed using a  
96 Coulter Counter (Multisizer 3) (Bianchi et al., 1999) with a 200  $\mu\text{m}$  aperture. The set-up was adapted  
97 following Moffa-Sanchez et al. (2015). The measurement error in the sortable silt mean grain size  
98 ( $\overline{SS}$ ) was 0.48  $\mu\text{m}$  (1 S.D., n=8).

### 99 2.2.2 Ice-rafted Debris

100 Counts of terrigenous grains  $>300 \mu\text{m}$  (used as a proxy for coarse IRD) were made every 1cm in order  
101 to determine potential changes in the source of sediment and the effect on  $\overline{SS}$ . Ice-rafted debris  
102 comprises all grain sizes but we use counts of grains  $>300 \mu\text{m}$  as a proxy for IRD because grains in  
103 this fraction are unlikely to be transported by other processes.

104 No obvious gravitational down-slope deposits were observed in the core, suggesting no influence  
105 from downslope transport that could have otherwise emplaced sediment unmodified by current  
106 transport at the site. Shards of Southern Andean volcanic ash or tephra have the potential to be  
107 transported significant distances by the south-westerly winds (SWWs), therefore grains of tephra  
108 were not counted.

### 109 2.2.3. Alkenone-derived Sea Surface Temperatures

110 Sea surface temperatures were calculated from the  $U_{37}^K$  index (Prahl et al., 1988) from alkenone  
111 analysis of core GC528 with an average sample resolution of 250 years. Lipids were extracted from  
112  $\sim 3$  g of homogenised, freeze-dried sediment using a CEM microwave system with 12 mL of  
113 Dichloromethane (DCM):MeOH (3:1, v/v) (Kornilova and Rosell-Melé, 2003). Internal standards were  
114 added for quantification (5 $\alpha$ -cholestane, dotriacontane and tetracontane). The relative abundances  
115 of di-, tri-, and tetra-unsaturated  $C_{37}$  alkenones were measured with a Trace Ultra gas  
116 chromatograph directly coupled to a Thermo DSQ single quadrupole mass spectrometer, fitted with  
117 a programmed temperature vaporising (PTV) injector. The target m/z were: 300 (nonadecanone),  
118 544 ( $C_{37:4}$ ), 546 ( $C_{37:3}$ ), 548 ( $C_{37:2}$ ), 560 ( $C_{38:3Et}$  and  $C_{38:3Me}$ ), 562 ( $C_{38:2Et}$  and  $C_{38:2Me}$ ), 564 and 578 ( $C_{36}$

119 alkyl alkenoates) (Rosell-Mele et al., 1995). Several samples were split and extracted separately to  
120 determine the procedural error of  $U_{37}^K = \pm 0.034$  ( $n=12$ ; equating to an error in SST  $\pm 1.2^\circ\text{C}$ ). The  
121 Prah et al., (1988)  $U_{37}^K$ -SST calibration produced the best match between the surface sample and  
122 modern annually-averaged sea surface temperatures at site GC528. This is because the Prah et al.,  
123 (1988) calibration is based on the  $U_{37}^K$  index (as opposed to the  $U_{37}^{K'}$ ), which includes  $C_{37:4}$ . This  
124 alkenone is abundant in high latitude regions and it has been shown that the  $U_{37}^K$  index provides  
125 more robust SST reconstructions in high Southern latitudes than  $U_{37}^{K'}$  (Ho et al., 2012).

#### 126 2.2.4. $\delta^{13}\text{C}_{\text{TOC}}$ and C/N ratio

127 Total organic carbon  $\delta^{13}\text{C}_{\text{TOC}}$  and C/N ratio are used here to track changes in surface ocean  
128 productivity and organic carbon source. Decarbonated samples (at 5 cm resolution) were measured  
129 for organic carbon content following the method described in Könitzer et al., (2012). Percentage  
130 carbon and nitrogen and  $\delta^{13}\text{C}_{\text{TOC}}$  analysis were performed by combustion on pre-weighed samples  
131 in an online system comprising a Costech ECS4010 elemental analyser (EA) coupled with a VG  
132 TripleTrap and a VG Optima dual-inlet mass spectrometer at the NERC Isotope Geosciences  
133 Laboratory. Each analytical run contained 10 replicates of the internal NIGL standard BROCC2 and 2  
134 replicates of the external standard SOILB.  $\delta^{13}\text{C}_{\text{TOC}}$  is reported relative to the VPDB standard, with a  
135 precision of 0.1‰ (1 S.D.).

#### 136 2.3. Numerical Modelling

137 A numerical model is used to determine the effect of a change in sea level on bottom current flow  
138 speeds. The numerical model (Princeton Ocean Model, Blumberg and Mellor, 1987) is a regional  
139 nested implementation of the Regional Ocean Modeling System. At the base there is a parent  
140 model, which extends from  $20^\circ\text{N}$  to  $70^\circ\text{S}$  and from  $180^\circ\text{E}$  to  $180^\circ\text{W}$  with a horizontal resolution of  $1/4^\circ$ .  
141 The parent model is nudged to the monthly mean climatological values of Simple Ocean Data  
142 Assimilation (SODA) at its northern (open) boundary. Nested into this parent model there is a child  
143 model, which covers all the southwestern Atlantic and southeastern Pacific sectors with a horizontal  
144 resolution of  $1/12^\circ$ . The nested model configuration is forced with climatological mean wind stress  
145 forcing derived from the ERA-Interim data set. Surface heat and freshwater fluxes are derived from  
146 the COADS dataset. See Combes and Matano 2014 and Palma et al. 2008 for details.

147 An "LGM" sea level simulation was run such that the only difference from the control was a 120 m  
148 reduction in sea level. Note that this "LGM" simulation does not take into account topographic  
149 changes related to isostatic adjustment. The LGM and control simulations were spun-up to  
150 dynamical equilibrium and run in diagnostic mode for 5 model years. Average values of the last year  
151 of the diagnostic run are used in the present analysis.

152 3. Results

153 3.1 Grain size analysis

154 The  $\overline{SS}$  at site GC528 almost doubles across the last deglaciation, from a minimum of 18.2  $\mu\text{m}$  at 19-  
155 18 ka to a maximum of 34.7  $\mu\text{m}$  at 1 ka [Figure 2b]. There are two step-wise changes in  $\overline{SS}$  across the  
156 deglaciation; (i) between 21-19 ka,  $\overline{SS}$  decreases by 5.2  $\mu\text{m}$ , (ii) between 14.5-14.0 ka,  $\overline{SS}$  increases  
157 by 5.0  $\mu\text{m}$ . After 10 ka, there is a steady increase in  $\overline{SS}$  spanning the entirety of the Holocene.

158 There is a  $\overline{SS}$ -bottom current flow speed calibration for the Scotia – Weddell Sea region ( $SS =$   
159  $0.59U + 12.24$ ) based on six points for which the sensitivity is 1.69  $\text{cm s}^{-1}/\mu\text{m}$ . However the greater  
160 confidence in the universal sensitivity of sortable silt mean grain size to bottom current flow speed  
161 based on 24 points of  $1.47 \pm 0.20 \text{ cm s}^{-1}/\mu\text{m}$  (by Coulter Counter) (McCave et al., submitted) is  
162 preferred. The total deglacial change in  $\overline{SS}$  of 16.5  $\mu\text{m}$  (34.7-18.2  $\mu\text{m}$ ) implies a change in bottom  
163 current flow speeds of 19.8-26.4  $\text{cm s}^{-1}$ . Given that the largest grains in the silt size fraction (60  $\mu\text{m}$ )  
164 transition into an erosion regime in flow velocities greater than 25  $\text{cm s}^{-1}$ , the magnitude of this  
165 deglacial change in  $\overline{SS}$  must correspond to an increase in bottom current velocity from  $<5 \text{ cm s}^{-1}$  to  
166  $\sim 20 \text{ cm s}^{-1}$  (using the lower limit of sensitivity).

167

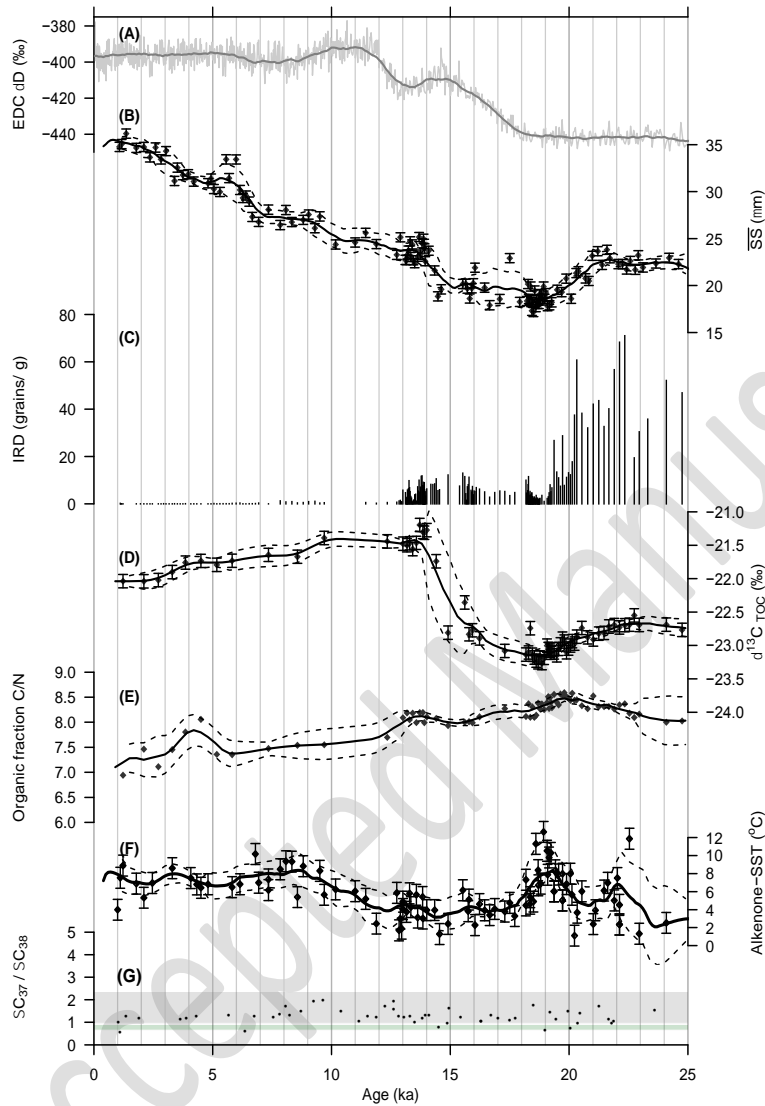
168 3.2 Fidelity of  $\overline{SS}$  as record of bottom water flow

169 Several processes act on glacial-interglacial timescales that could affect the sedimentation at GC528,  
170 such as changes in flow strength, sea level and ice-rafting, which we discuss here.

171 Reconstruction of the LGM Patagonian coastline (based on modern bathymetry) places it 200 km  
172 closer to GC528 than it is today (Figure S1), potentially increasing sediment supply. This could impact  
173 on the reliability of  $\overline{SS}$  as a bottom current flow speed proxy if the rate of direct sediment  
174 introduction was faster than the current could rework. The sediment mass accumulation rate at  
175 GC528 was higher during the LGM than the Holocene (Figure S1b), likely reflecting a closer sediment  
176 source during glacial times as a result of the sea level lowstand. However, it is interesting to note  
177 that the mass accumulation rate at GC528 does not decrease linearly with increasing sea level across  
178 the deglaciation, suggesting that any relationship between sea level and sediment supply to GC528 is  
179 not straightforward. Increased rates of sea level rise at 20-19 ka and 14.5-13 ka coincide with  
180 elevated accumulation rates at GC528 (Figure S1b-c), perhaps suggesting that the initial flooding of  
181 exposed shelf may have affected sediment supply to the slope.

182 At high latitudes, ice-rafted sediment provides additional material to the core site with significant  
183 fluctuations on glacial-interglacial timescales. At site GC528, high concentrations of IRD are observed

184 during the LGM [Figure 2c]. This is consistent with acoustic images of scours on the seafloor in the  
 185 region suggesting the presence of icebergs in the past (Brown et al., 2017). The concentration of IRD  
 186 at GC528 rapidly decreases between 20-19 ka, corresponding to a decrease in  $\overline{SS}$  (Figure S2b).



187  
 188 *Figure 2: Deglacial grain size analysis, organic carbon and biomarker records from site GC528 in the*  
 189 *southwest Atlantic. (A) EPICA Dome C (EDC)  $\delta D$  record on the AICC2012 age scale (Veres et al., 2013);*  
 190 *(B) Mean sortable silt grain size ( $\overline{SS}$ ); (C) Counts of grains  $>300 \mu m$ , used as a proxy for IRD; (D) Total*  
 191 *organic carbon (TOC)  $\delta^{13}C$ ; (E) Organic carbon C/N ratio; (F) Alkenone-derived SST based on the  $U^{k}_{37}$*   
 192 *index (Prahl et al., 1988); (G) Total  $C_{37}:C_{38}$  alkenones used here to track changes in the alkenone-*  
 193 *producing community. Grey and green bars show the typical range of *E.huxleyi* and *G.oceanica**  
 194  *$C_{37}:C_{38}$  ratio based on culture studies (Volkman et al., 1995). In each record, the  $2\sigma$  analytical*  
 195 *precision is shown by the error bars, and a 1500 yr moving average and  $1\sigma$  moving standard*  
 196 *deviation of each record is shown by the solid line and dashed lines respectively.*

197 Do the variations in the sedimentation rate across the last deglaciation reduce confidence in  $\overline{SS}$  as  
198 an indicator of bottom current flow speed? The key assumption underlying the  $\overline{SS}$  proxy is that the  
199 sediment must be current sorted (McCave et al., 1995). Lamy et al., (2015) used the correlation  
200 between  $\overline{SS}$  and %SS to demonstrate current sorting at sites within the Drake Passage. In GC528, the  
201 cross-plot of  $\overline{SS}$  and %SS (measured on a subset of the samples, with a temporal resolution of 500  
202 years) reveal that the sortable silt fraction of all sediments within GC528 has been current sorted,  
203 even within intervals that have been strongly influenced by IRD (Figure S2a), and there is no  
204 correlation between  $\overline{SS}$  and IRD concentration (Figure S2b). Therefore, we are confident that the  
205  $\overline{SS}$  presented here can be interpreted as a reliable record of bottom current flow speeds.

### 206 3.3 Source of IRD in the southwest Atlantic

207 Variations in IRD concentrations occur across the last deglaciation at site GC528 (Figure 2c). The two  
208 most significant potential source regions of this IRD are Patagonia and Antarctica. Acoustic imaging  
209 of the shelf sediments north of the Falkland islands have identified iceberg scours at present-day  
210 water depths of 240-480m (Brown et al., 2017). These authors argue that the depth of these scours  
211 requires large icebergs that could only have been derived from Antarctica. The anti-clockwise nature  
212 of the Antarctic coastal current means that icebergs calving off Antarctic glaciers typically  
213 accumulate within the Weddell Sea (Stuart and Long, 2011). From the Weddell Sea, most of the  
214 Antarctic icebergs escape into the ACC via "Iceberg Alley". Weber et al. (2014) identified several  
215 large iceberg discharge events from the Weddell Sea during the last deglaciation. However,  
216 consistent with icebergs drifting eastwards with the ACC from the Scotia Sea region, the timing of  
217 these iceberg discharge events (18-12 ka) do not coincide with the maximum IRD concentration at  
218 site GC528 (21-19 ka) (Figure S3), indicating that the source of IRD at GC528 was distinct from the  
219 Scotia Sea. We consider it likely that the dominant source of IRD deposited at GC528 was derived  
220 from marine-terminating glaciers on the west coast of Patagonia and transported through the Drake  
221 Passage. However, an exclusively Patagonian origin of IRD in this region is inconsistent with the  
222 inference of Brown et al. (2017) based on iceberg size, suggesting that icebergs sourced from East  
223 Antarctic may also have approached our site via the Drake Passage. A detailed IRD provenance study  
224 would be required to further test this hypothesis.

### 225 3.3 Productivity changes at site GC528

226 The  $\delta^{13}C_{TOC}$  reflects variations in both surface water productivity and source of organic matter,  
227 whereas the C/N ratio is primarily driven by the organic carbon source. In core GC528, organic  
228 carbon  $\delta^{13}C_{TOC}$  increases from values ranging between -23.0 to -22.6 ‰ prior to 15 ka, to -21.5 to -  
229 21.0 ‰ after 14 ka [Figure 2d]. In contrast the C/N ratio gradually decreases across the deglaciation



230 and Holocene with no marked shift in the C/N ratio at 15-14 ka [Figure 2e]. Taken together, we  
231 suggest the shift at 15-14 ka to more positive  $\delta^{13}\text{C}_{\text{TOC}}$  reflects a change in surface ocean productivity.

### 232 3.4 Alkenone-derived SST

233 Alkenone-derived SST across the last deglaciation is highly variable [Figure 2e]. The Holocene (10-0  
234 ka) average SST ( $7.6 \pm 2.0$  °C) is in good agreement with modern annual average SSTs at the core  
235 location. In contrast to other southern hemisphere alkenone records (e.g. Caniupán et al., 2011;  
236 Kaiser et al., 2005), the LGM (19-22 ka) average alkenone-derived SST at GC528 is relatively warm  
237 ( $7.0 \pm 3.9$  °C). However, this average value masks the large fluctuations that are apparent in the  
238 alkenone-SST record across the LGM. The LGM SSTs fluctuate between a minimum of 1.3°C at 25-23  
239 ka and a maximum of 8°C at 19 ka, and there are two intervals spanning the end of the last glacial  
240 period (20-18.5 ka and 23-22 ka) during which SSTs in the southwest Atlantic were elevated by 4-6°C  
241 above the glacial mean. Replicate analyses on samples over this interval confirm that these warm  
242 LGM temperature signals are robust. In the following, we evaluate factors that may result in the  
243 elevated LGM alkenone-derived SSTs.

### 244 3.5 Fidelity of alkenone- $U_{37}^K$ as record of sea surface temperature

245 Variations in the dominant alkenone-producing haptophyte could require the use of different  
246 regressions between  $U_{37}^K$  and SST. The abundance of  $\Sigma\text{C}_{37}$ :  $\Sigma\text{C}_{38}$  alkenones within a sediment sample  
247 has been used to identify shifts in the dominant alkenone-producing haptophyte population  
248 (McClymont et al., 2005). We identify no significant shift in the  $\Sigma\text{C}_{37}$ :  $\Sigma\text{C}_{38}$  ratio over the interval  
249 studied [Figure 2f] with values averaging 1.16, in the range of *Emiliana huxleyi* (0.91-2.26) rather  
250 than the other dominant alkenone-producing haptophyte *Gephyrocapsa oceanica* (0.59-0.81)  
251 (Volkman et al., 1995). This suggests that no change in the dominant alkenone producing  
252 haptophyte population occurred, and thus the  $U_{37}^K$ -SST relationship should have remained constant.

253 Preferential degradation of components with a greater degree of unsaturation may bias the  
254 alkenone-SST record towards warmer values (Flügge, 1997). We consider the percentage of the cold  
255 tetra-unsaturated  $\text{C}_{37:4}$  alkenone that would need to be removed in order to produce LGM SSTs as  
256 low as during the late deglaciation period (2.2°C at 11.9 ka). We find that to account for a diagenetic  
257 bias of 6°C, at least 70% of the 'original'  $\text{C}_{37:4}$  would have to be removed from the samples. Such a  
258 significant amount of alteration has not been observed experimentally or within sediments studied  
259 from this time period (Flügge, 1997).

260 Advection of warm water alkenones has been used to explain a warm LGM alkenone-SST signal in  
261 some regions of the ocean. Modern alkenone studies from sites influenced by the Falkland Current  
262 (Benthien and Müller, 2000) demonstrate that alkenone-derived SSTs from this region are biased

263 towards colder temperatures as a result of strong northward transport by the Falkland Current and  
264 deep western boundary current. However core-top alkenone-SST data from site GC528 (7.7 °C)  
265 shows good correlation with modern SSTs suggesting that advection does not strongly bias the  
266 alkenone-SST signal at this site.

267 Reworking of alkenones from older warm intervals (such as the Eemian) could overprint the original  
268 alkenone-SST and bias the alkenone signal to warmer temperatures. However, we do not believe  
269 this to be a significant issue at site GC528 because (i) neither the TOC or the alkenone  
270 concentrations during the two “warm” intervals during the LGM are significantly higher than the  
271 LGM average [Figure S3b-c], and (ii) other proxies such as planktonic  $\delta^{18}\text{O}$  [Figure S3d] show no  
272 evidence of reworking. In addition, the spatial distribution of “warm” alkenone-derived LGM SST  
273 records is globally distributed (Barrows et al., 2011). If all the sites were influenced by older  
274 reworked alkenones, they would all have to be simultaneously affected by (specifically warm)  
275 reworked alkenones during the LGM only. This seems an improbable explanation.

276 Changes in the seasonality of alkenone production can affect the temperatures recorded by the  
277 alkenones. In high latitude regions, the limitation of light and the extreme surface conditions restrict  
278 alkenone production to a short summer growth season (Ternois et al., 2000). Site GC528 is located in  
279 the sub-Antarctic, and is sufficiently far north that it is not light limited. However, could there be  
280 other processes in play during the LGM that affects the seasonality of alkenone production? Whilst it  
281 is unlikely that sea ice was able to accumulate (even seasonally) across the Drake Passage, there  
282 exist very indirect arguments supporting the idea that sea ice may have been present between the  
283 Falkland Islands and Argentina during the LGM (Austin et al., 2013); however, we find no evidence of  
284 any sea ice biomarkers (i.e. highly-branching isoprenoids (Collins et al., 2013)) in the glacial samples  
285 of GC528. Alternatively, the accumulation of large icebergs in an “iceberg graveyard” around the  
286 Falkland shelf (Brown et al., 2017) could have generated shallow meltwater stratification in the  
287 surface ocean, potentially biasing summer SSTs (Peck et al., 2008). High IRD concentrations  
288 coincident with both apparent warming events lend weight to this hypothesis [Figure 2c].

289 Despite our concern that seasonality could have led to a warm bias in the glacial alkenone SST at site  
290 GC528, a global comparison of seasonality in alkenone flux demonstrated that at a global scale, the  
291 mean annual SST signal still dominates the sedimentary record (Rosell-Melé and Prahl, 2013).  
292 Furthermore, where high latitude seasonality in alkenone production has been shown (Conte et al.,  
293 2006), the bias relative to the expected mean annual SST was only 2.5°C. Subtracting this value from  
294 our glacial-stage warm intervals does not compensate the 4 °C anomalies relative to the other  
295 samples; thus, the intervals of warming remain. As we show later (Section 4.1), seemingly logical  
296 spatial trends in SSTs can be inferred from the comparison of this SST record with other alkenone-

297 SST records in the Drake Passage region (see Section 4.1). We therefore argue that whilst a  
298 seasonality overprint of the glacial alkenone-SST record could have contributed to the magnitude of  
299 the warmings, the overall pattern in SSTs remains robust.

#### 300 4. Discussion

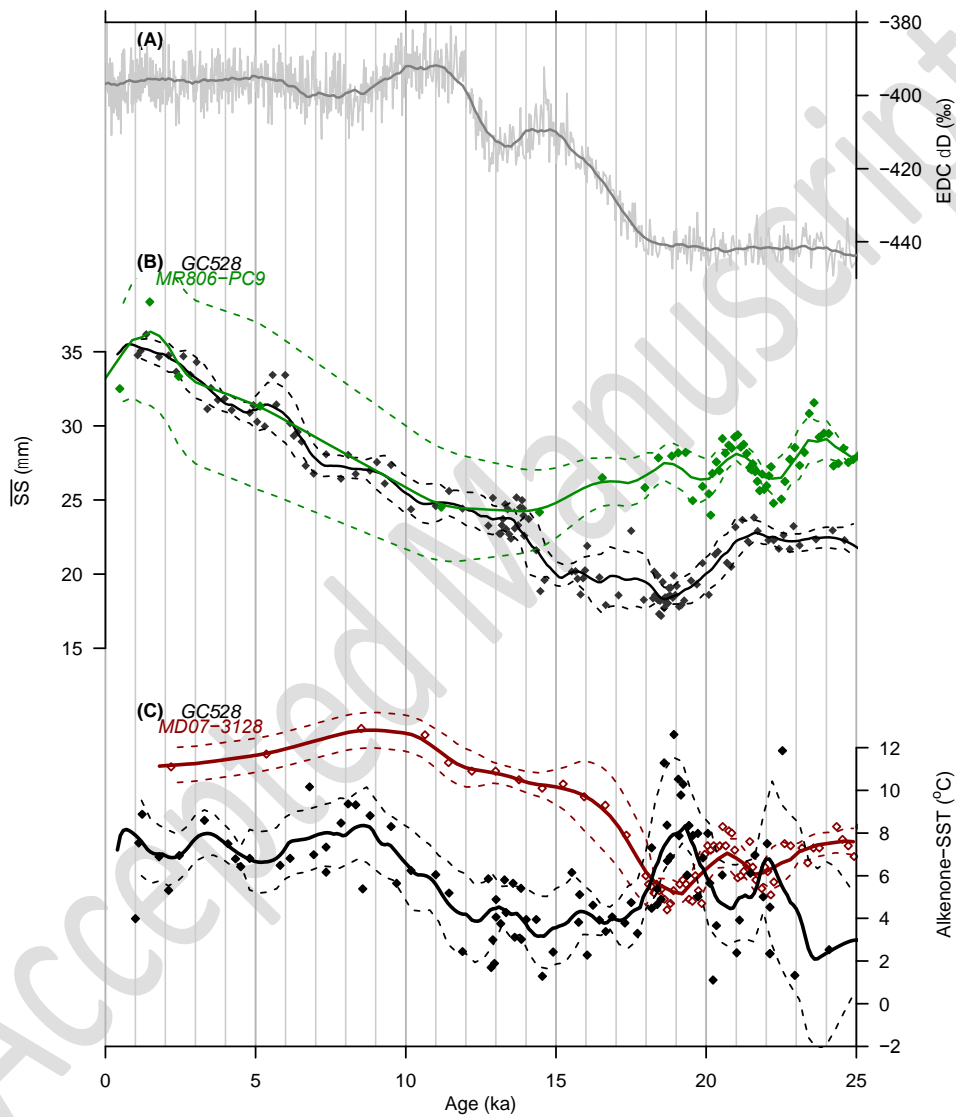
##### 301 4.1 The 15-14 ka event

302 The  $\overline{SS}$  record from site GC528 shows a step-wise increase in bottom current flow speeds ( $\Delta U = 6.4$   
303  $\text{cm s}^{-1}$ ) at 14.5-14 ka [Figure 2b]. Coupled with the change in bottom current velocity, there is  
304 evidence of a significant increase in  $\delta^{13}\text{C}_{\text{TOC}}$  [Figure 2d], potentially reflecting increased surface ocean  
305 productivity. Today, the Falkland Current (the most northerly ACC jet associated with the SAF) acts  
306 as the primary source of nutrients to the surface ocean above site GC528, supporting high  
307 concentrations of chlorophyll along the shelf break. While the Falkland Current remains in-situ,  
308 surface productivity is relatively unresponsive to changes in dust flux (unlike other sub-Antarctic  
309 sites). This idea is supported by our record of  $\delta^{13}\text{C}_{\text{TOC}}$ , which shows little response to the well-known  
310 decrease in dust between 18-17 ka (Lambert et al., 2008). This indicates that the prominent increase  
311 in  $\delta^{13}\text{C}_{\text{TOC}}$  at 14.5-14 ka was likely driven by reorganisation of the oceanic currents in the region.  
312 Oceanic current reorganisation would impact the supply of nutrients and/or the thermohaline  
313 properties of the surface ocean, affecting surface productivity. Furthermore, reorganisation would  
314 impact the bottom current speeds, so would be expressed in the  $\overline{SS}$  record.

315 Understanding the nature of the inferred change in ocean circulation at 14.5-14 ka requires  
316 comparison with other sites in the region. Site MR806-PC9 is located at the northern margin of the  
317 Drake Passage [Figure 1a], and is today immediately upstream of site GC528 within the jet  
318 associated with the SAF [Figure 1b]. Comparison of the  $\overline{SS}$  records between site GC528 and MR806-  
319 PC9 (Lamy et al., 2015) reveals a remarkable similarity in bottom current speed at the two sites  
320 between 14-0 ka [Figure 3b]. In contrast, prior to 14 ka, there was divergence between the two  $\overline{SS}$   
321 records [Figure 3b], with faster bottom current flow speeds in Drake Passage than on the South  
322 Falkland slope.

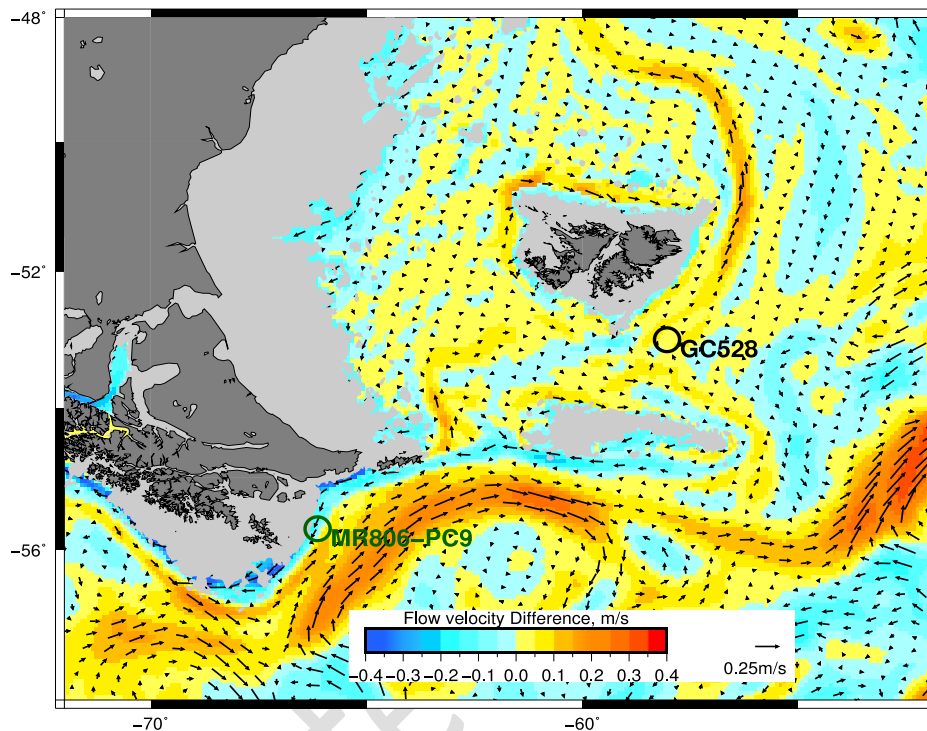
323 The fact that sites GC528 and MR806-PC9 presently lie within the core of the main SAF jet [Figure  
324 1b] and have similar bottom current flow speeds over 14-0 ka [Figure 3b] suggests a common  
325 response to changes in the intensity of the SAF jet. Both records suggest strengthening of the SAF jet  
326 through the Drake Passage over the late deglaciation and Holocene (which we discuss in Section  
327 4.2). In contrast, the disparity in bottom current flow speeds prior to 14 ka - with faster flow speeds  
328 in Drake Passage relative to the downstream site - could be the product of one of two different  
329 scenarios; (i) a lower glacial sea level meant that the SAF did not cross the topographic high of the

330 North Scotia Ridge and thus site GC528 was 'shielded' from the influence of the SAF, or (ii) the  
 331 Southern Ocean frontal system shifted northwards relative to its current position such that the SAF  
 332 did not extend through Drake Passage but instead was truncated by South America, analogous to  
 333 the present Sub-Tropical Front. The faster flow speed at MR806-PC9 may then be the result of  
 334 proximity to a more northerly position of the Polar Front.



335  
 336 *Figure 3: Comparison of proxy records from GC528 with upstream sites. (A) EPICA Dome C (EDC) δD*  
 337 *record on the AICC2012 age scale (Veres et al., 2013); (B) Mean sortable silt grain size ( $\overline{SS}$ ), GC528*  
 338 *(black) and MR806-PC9 (green; Lamy et al., 2015); (C) Alkenone-derived SST records from upstream*  
 339 *(MD07-3128 - red, Caniupán et al. 2011) and downstream (GC528 - black) of the Drake Passage. A*  
 340 *1500 yr moving average and 1σ moving standard deviation of each record is shown by the solid line*  
 341 *and dashed lines respectively.*

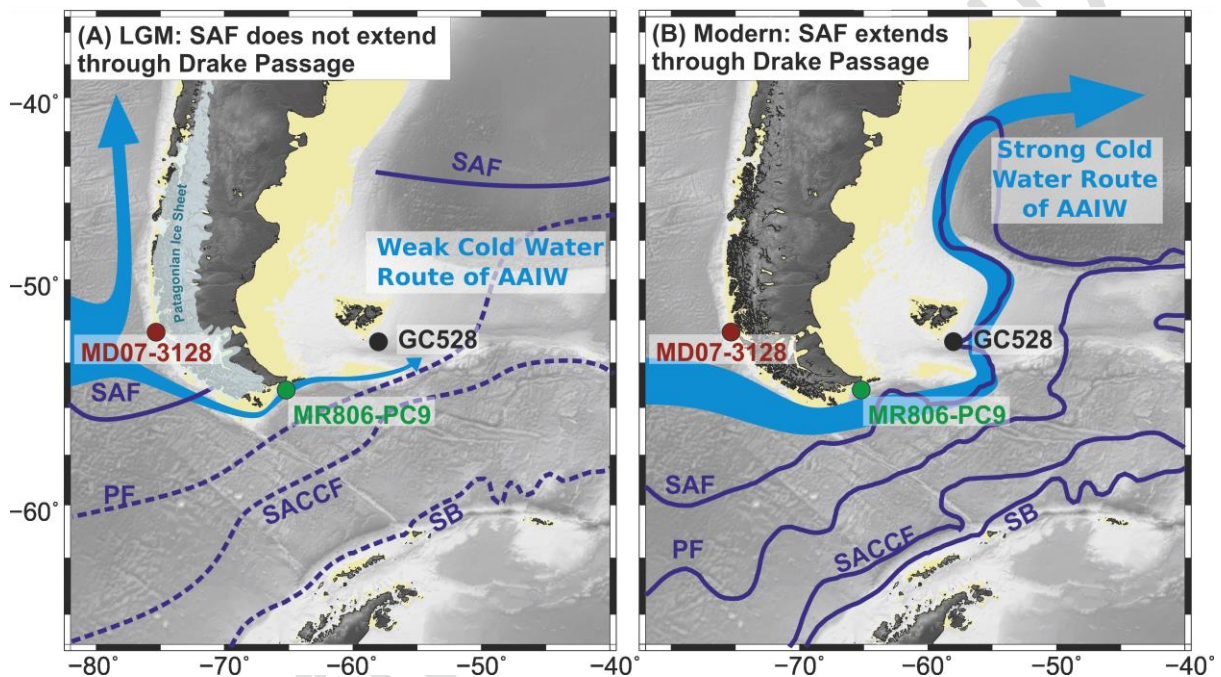
342 In order to test Scenario 1 (a lower sea level shielded GC528 from the SAF), we modelled the effect  
 343 of a lower sea level on bottom current flow speeds. The model predicts an overall increase in  
 344 bottom current flow within the Drake Passage [Figure 4]. This increase is because the ACC is an  
 345 equivalent barotropic jet and therefore, bottom current velocities are inversely proportional to the  
 346 depth of the fluid. In contrast to the general strengthening within the Drake Passage, the model  
 347 predicts a decrease in bottom current flow speeds of 10-15  $\text{cm s}^{-1}$  at site MR806-PC9 [Figure 4].



348  
 349 *Figure 4: Model simulations of changes in bottom water flow speeds as a result of a lowering of sea*  
 350 *level. Plot shows the relative change in bottom current flow velocity as a result of a -120m reduction*  
 351 *in sea level. A reduction in bottom current velocity is highlighted by the blue colours. Green and black*  
 352 *open circles show the position of MR806-PC9 (in Drake Passage) and GC528 (south of the Falkland*  
 353 *Islands) respectively. Pale grey shows the model coastline in the low sea level scenario.*

354 This is driven by the development of a frictional recirculation cell that occupies the space between  
 355 the continent and the intensified offshore flow, and is highly dependent on the model configuration,  
 356 and is therefore not a robust prediction. At site GC528, the model predicts an increase of 6  $\text{cm s}^{-1}$  in  
 357 northward advection of bottom water during sea level lowstands [Figure 4]. This predicted increase  
 358 in transport at GC528 is driven by a reduction in on-shelf transport, resulting in an increase in  
 359 transport along the shelf-break. Because the Patagonian shelf is so expansive, a reduction in sea  
 360 level results in a large reduction in on-shelf transport (and subsequent increase in shelf-break

361 transport) relative to the minor reduction in the transport across the North Scotia Ridge. Therefore a  
 362 relative strengthening of bottom currents is predicted at GC528. The model predictions are  
 363 inconsistent with our  $\overline{SS}$  reconstructions across the 15-14 ka transition, which suggest a significantly  
 364 weaker bottom current before 15 ka at site GC528 and a stronger bottom water flow at MR806-PC9.  
 365 Whilst we emphasise the uncertainty in the model prediction at MR806-PC9, we are confident in the  
 366 model result at GC528. The discrepancy between the model prediction and the  $\overline{SS}$  reconstructions  
 367 implies that sea level change is not the driver of the change in bottom current flow speeds observed  
 368 in the records at GC528 (and possibly also MR806-PC9). Instead, oceanographic changes other than  
 369 eustatic sea level change must have controlled the observed bottom current speed changes.

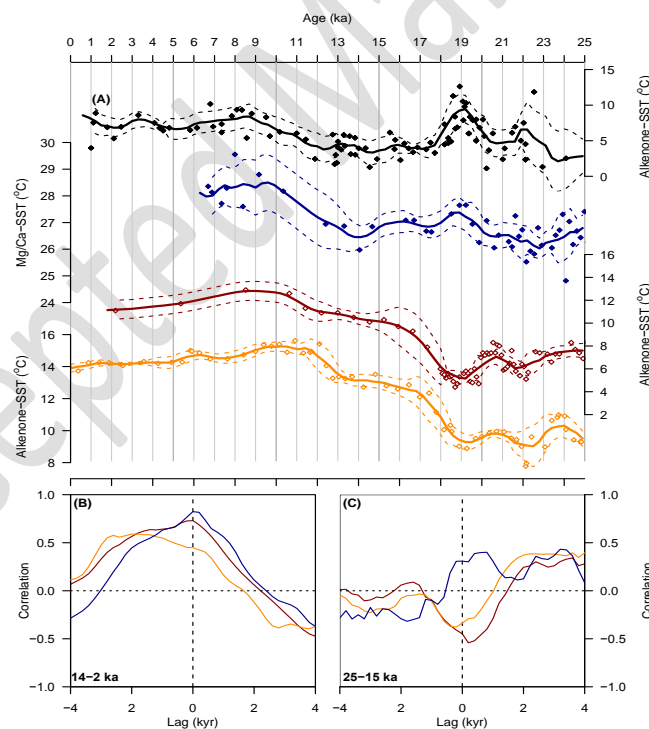


370  
 371 *Figure 5: Schematic of changes in ACC frontal jets from the last glacial period to the Holocene with*  
 372 *inferred inter-basinal exchange between Pacific and Atlantic. (A) Glacial ACC flow showing SAF*  
 373 *located northwards of its present position and little inter-basinal exchange; (B) Holocene ACC flow*  
 374 *showing the SAF extending through the Drake Passage and enhanced inter-basinal exchange. The*  
 375 *positions of the ACC fronts are shown by the blue lines (more speculative locations denoted by*  
 376 *dashed lines). The “Cold Water Route” water shown by light blue arrow. SAF = Sub-Antarctic Front;*  
 377 *PF = Polar Front; SACCF = Southern Antarctic Circumpolar Current Front; SB = Southern Boundary*  
 378 *Front.*

379 An alternative hypothesis invokes a change in the position of the oceanic fronts. LGM front  
 380 reconstructions (e.g. Gersonde et al., 2005) suggest that the Southern Ocean fronts were located 5-  
 381 10° northward of their present position. We propose that during the last glacial and early deglacial  
 382 period (until 15 ka), the SAF did not extend through the Drake Passage but was instead truncated by

383 the South American continent (similar to the modern Sub-Tropical Front; Figure 5a). If the SAF did  
 384 not extend through the Drake Passage, slower bottom current flow velocities at both GC528 and  
 385 MR806-PC9 would be expected. The fact that bottom current flow speeds at MR806-PC9 are  
 386 significantly faster than GC528 prior to 15 ka [Figure 4b] suggests that this is not the entire story,  
 387 and may be influenced by a more northerly located Polar Front [Figure 5a] or a decrease in sea level  
 388 (given the model uncertainty at this location).

389 Support for the idea of a northward shifted SAF can be found in the Pacific-Atlantic SST phase  
 390 relationships over the last deglaciation. The comparison of alkenone-SST records from GC528 and  
 391 two sites upstream of the Drake Passage [Figure 1a], site MD07-3128 (Caniupán et al., 2011) and  
 392 ODP 1233 (Kaiser et al., 2005) reveals a striking SST anti-correlation prior to 15 ka [Figures 3c, 6c].  
 393 Intervals of warming downstream of the Drake Passage (e.g. 23-22 ka and 20-18 ka) coincide with  
 394 significant cooling upstream. From 14 ka onwards, this anti-phase relationship is absent [Figures 3c,  
 395 6b]. In contrast, planktonic Mg/Ca-derived SSTs downstream of GC528, at the Brazil Margin site GL-  
 396 1090 (24°S, 42°W; Santos et al., 2017) are in-phase with site GC528 throughout the last deglaciation  
 397 [Figure 6]. The idea of a “thermal see-saw” between the southeast Pacific and the southwest Atlantic



398  
 399 *Figure 6. (A) Sea surface temperature records from GC528 (black) and GL-1090 (blue, Santos et al.,*  
 400 *2017) from the southwest Atlantic, and sites MD07-3128 (red, Caniupán et al., 2011) and 1233*  
 401 *(orange, Kaiser et al., 2005) from the Chile Margin. (B) Cross-correlation between GC528 and MD07-*  
 402 *3128 (red), GC528 and 1233 (orange), and GC528 and GL-1090 (blue) for the interval 14-2 ka; (C)*  
 403 *Cross correlation for 25-15 ka, colours as in (B).*



404 during the last glacial and early deglacial period (25-15 ka) supports the inference of northward  
405 shifted SAF during the LGM and early deglaciation. In the southeast Pacific, SSTs are controlled by  
406 the balance between cold sub-Antarctic Surface Water of the ACC advected northeastwards and  
407 warm surface waters transported southwards by the Chilean Coastal Current (Strub et al., 1998).  
408 Similarly, the SSTs in the southwest Atlantic represent a balance between cold southern-sourced  
409 water transported through the Drake Passage (Talley, 1999) and warm northern-sourced water  
410 carried southwards via the Brazil Current (Peterson and Stramma, 1991). Hypothesising that the SAF  
411 was absent from the Drake Passage during the LGM, a significant proportion of the cold water  
412 transported via the ACC to the Chilean margin would be redirected northwards into the Pacific (Lamy  
413 et al., 2015). This results in a relative cooling in the southeast Pacific and warming in the southwest  
414 Atlantic [Figure 5a]. Note that, based on our hypothesis, we argue that the warm LGM SST records  
415 from the Brazil Margin (Santos et al., 2017) are the result of a reduction in cold water advected  
416 through the Drake Passage, rather than an increase in warm water advected south from the Equator.

417 The transition to in-phase SSTs upstream and downstream of Drake Passage at ~14 ka is consistent  
418 with the southward migration of the SAF to pass through the Drake Passage [Figure 5b]. A  
419 southward shift of the SAF would increase the inter-basin exchange of water between the Pacific  
420 and Atlantic, enabling temperature perturbations upstream of Drake Passage to be propagated  
421 rapidly to regions downstream of this gateway.

422 In summary, sortable silt, SST and  $\delta^{13}\text{C}_{\text{TOC}}$  records from GC528 suggest a significant change in ocean  
423 circulation in the southwest Atlantic at 15-14 ka. Comparison of bottom current flow speeds  
424 downstream and within the Drake Passage provides evidence for a significant reorganisation of the  
425 frontal structure in the Drake Passage region across this interval. In particular, we suggest that the  
426 SAF did not extend through the Drake Passage until 15-14 ka. Anti-phased alkenone-SST records  
427 upstream and downstream of the Drake Passage support the idea of a reduced inter-basinal  
428 connection prior to 15 ka.

#### 429 4.2 Strengthening of flow in the SAF after 14 ka

430 Bottom current flow speeds downstream (GC528) and within the Drake Passage (MR806-PC9)  
431 evidence a significant increase ( $\overline{\Delta SS}$  of  $11.5 \mu\text{m}$  suggests an increase of  $\sim 16 \text{ cm s}^{-1}$ ) since 14 ka. Given  
432 that both sites record a very similar  $\overline{SS}$  record throughout this period, we infer that both sites are  
433 responding to an in-situ increase in the strength of the jet associated with the SAF. A strengthening  
434 of the SAF is supported by  $\epsilon\text{Nd}$  records from the Brazil Margin (Howe et al., 2016), which show  
435 increasingly radiogenic Nd isotopic signatures across the Holocene, indicating a greater through-flow  
436 of Pacific-derived AAIW.

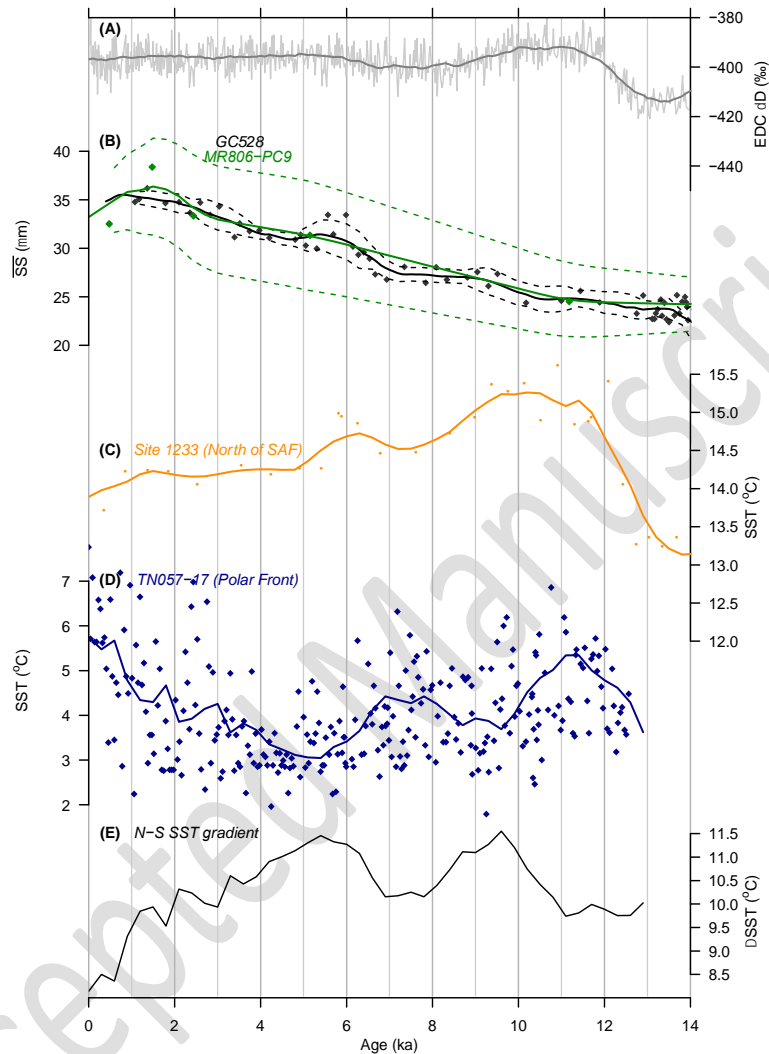


437 The cause of such a large increase in the strength of the SAF jet is difficult to determine. The density  
438 difference either side of a front results in a strong pressure gradient, which is balanced by the  
439 Coriolis force producing a strong eastward jet. At a basic level, a stronger density gradient across a  
440 front will strengthen the associated jet (Thompson, 2008). The SAF is the location where cold-fresh  
441 dense Antarctic-derived water subducts beneath less dense water to the north to form Antarctic  
442 Intermediate Water (Hartin et al., 2011). The increase in the strength of the jet associated with the  
443 SAF may thus be the result of an increase in the density contrast between sub-Antarctic Surface  
444 Water north of the SAF and Antarctic surface waters south of the SAF.

445 Proxy data of SSTs from north and south of the SAF do not provide strong support for the idea of an  
446 increased north-south temperature-driven surface density gradient during the Holocene. Sea surface  
447 temperature records of Antarctic surface water across the Holocene in the South Atlantic (Figure 7D;  
448 Nielsen et al., 2004) suggest an early Holocene warming followed by a cooler interval between 7-4  
449 ka, and a relative warming from 4 ka to the present. In contrast, SST records north of the SAF from  
450 the Chilean margin suggest an initial warming in the Early Holocene followed by a general cooling  
451 trend (Figure 7C; Kaiser et al., 2005). Over the course of the Holocene, there is significant fluctuation  
452 in the north-south SST gradient; however, the long-term Holocene trend suggests a general decrease  
453 in the SST gradient [Figure 7E]. Based on this evidence, we cannot attribute the increase in the  
454 intensity of the SAF jet to an increase in a density gradient driven by temperature across the front.  
455 Note that the sites that we have used to reconstruct the SST gradient in Figure 7 are not proximal to  
456 the SAF and so may not accurately reflect SST gradients in the vicinity of the SAF. Alternatively, there  
457 remains the possibility of salinity-driven changes related to ice-melt, but we have no data to  
458 examine this aspect, nor (to our knowledge) are there any proxy data reconstructions of salinity  
459 across the SAF. However, it should be noted that the melt-related salinity gradients in the Southern  
460 Ocean were probably at a maximum during the deglaciation (18-12 ka) when the majority of ice was  
461 lost from Antarctica and Patagonia, and not during the Holocene.

462 Finally, based on current understanding of the ACC, we observe that it is difficult to determine how  
463 changes in the intensity or position of the south westerly winds (SWW) might drive changes in the  
464 strength of the SAF jet. The SWWs transfer momentum into the surface ocean of the ACC, which sets  
465 up the barotropic component of flow (e.g. Allison et al., 2010). However, the exact relationship  
466 between the overlying wind forcing and the response of the ACC remains a matter of debate and is  
467 model dependent (Hogg et al., 2008 and references therein). Eddy compensation and eddy  
468 saturation result in non-linear responses of the ACC to changes in wind forcing, and jets are a finer  
469 scale that is not often well resolved in models. Furthermore, even if the response of the ACC could  
470 be predicted, proxy reconstructions of SWW strength show that the SWWs did not increase

471 monotonically across the Holocene (Lamy et al., 2010). On balance, wind stress cannot adequately  
 472 explain the seemingly linear increase in bottom current flow speeds suggested by data presented  
 473 here



474

475 *Figure 7: Reconciling the increase in strength of the SAF with changes in SST gradients over the*  
 476 *Holocene. (A) EPICA Dome C (EDC)  $\delta D$  record on the AICC2012 age scale (Veres et al., 2013); (B)*  
 477 *Mean sortable silt grain size, GC528 (black) and MR806-PC9 (green; Lamy et al., 2015); (C) Alkenone-*  
 478 *SST record from the Chilean Margin, north of the SAF (orange; ODP site 1233, Kaiser et al., 2005); (D)*  
 479 *Diatom transfer function based SST reconstruction from the Atlantic Sector of the Southern Ocean, at*  
 480 *the Polar Front (blue; Core TN057-17, Nielsen et al., 2004); (E) Difference between the two SST*  
 481 *records (C and D), used here as an indication of the density gradient across the SAF. A 1500 yr moving*  
 482 *average and  $1\sigma$  moving standard deviation of each record is shown by the solid line and dashed lines*  
 483 *respectively.*

484 In summary, the increase in bottom current velocities at sites in the Drake Passage and on the South  
485 Falkland slope since 14 ka suggests an increase in the strength of the SAF jet. However, the  
486 underlying cause of the increase in SAF jet strength remains enigmatic. Improved knowledge of sea  
487 surface salinity and temperature in the Drake Passage region could provide a key to understanding  
488 the increase in SAF jet flow speed across the Holocene.

#### 489 4.3 Implications for the Atlantic Meridional Overturning Circulation (AMOC)

490 A key idea presented here is that of a thermal seesaw between the southeast Pacific and southwest  
491 Atlantic during the last glacial period and early deglacial (25-15 ka). This, we argue, was related to a  
492 reduction in the interbasinal connection via the Drake Passage as a result of a northward shifted SAF.  
493 The following discussion concerns the wider effect of these changes on ocean circulation.

494 The relative proportion of water flowing into the Atlantic basin via the Cold and Warm Water Routes  
495 affects the thermohaline properties of the shallow northward return flow. Extension of the SAF  
496 through the Drake Passage would have transmitted a greater volume of cold SAMW into the  
497 southwest Atlantic via Drake Passage, with potential consequences for global ocean circulation.

498 The onset of the southward shift of the SAF at 15-14 ka is synchronous with a 'spin-up' of the AMOC  
499 during the Bølling-Allerød interstadial (McManus et al., 2004; Skinner et al., 2013). This AMOC spin-  
500 up has commonly been interpreted to reflect changes in North Atlantic freshwater forcing, but the  
501 flow of water through the Drake Passage might also have played a role. Reduced throughput of cold  
502 low-salinity SAMW during the LGM would result in denser Atlantic AAIW (relative to today). If the  
503 density of Atlantic AAIW advected into the North Atlantic exceeds the density of NADW, then AMOC  
504 is potentially unstable (Keeling and Stephens, 2001). In contrast, a southward shift of the SAF at 15-  
505 14 ka would increase the transport of low-salinity SAMW into the Atlantic and decrease the density  
506 of AAIW relative to NADW, producing a more stable AMOC (Keeling and Stephens, 2001), and could  
507 explain the re-invigoration in AMOC observed during the Bølling-Allerød interstadial (McManus et  
508 al., 2004; Skinner et al., 2013). Support for this hypothesis comes from modelling studies (Weaver et  
509 al., 2003) which show that, given an initial circulation state in which the density of AAIW is greater  
510 than that of NADW, it is possible to spin up AMOC circulation by freshening AAIW in the vicinity of  
511 the Drake Passage. In this scenario, Drake Passage through-flow would act as a driver of AMOC  
512 circulation.

#### 513 5. Conclusion

514 In this study, detailed grain size data and SST records from sites along the northern margin of Drake  
515 Passage were used to determine changes in the flow and frontal structures within the Drake Passage

516 since the LGM. In particular, we focus on the interval between 15-14 ka when an increase in bottom  
517 water current speeds is accompanied by increased in  $\delta^{13}\text{C}_{\text{TOC}}$  in the southwest Atlantic, indicating  
518 significant reorganisation of the currents. Comparison of bottom current flow speeds in the  
519 southwest Atlantic under the influence of the SAF jet to an upstream site in the Drake Passage  
520 reveals very similar trends after 14 ka, indicating that both sites are responding to changes in the  
521 strength of the SAF jet. In contrast, prior to 15 ka, bottom current speeds at the two sites are  
522 dissimilar. We propose that during the interval prior to 15 ka, the SAF did not extend through Drake  
523 Passage but instead lay further north and was truncated by South America, similar to the modern  
524 STF. This hypothesis is supported by alkenone-based SSTs upstream and downstream of the Drake  
525 Passage that suggest through-flow via the Cold Water Route during the last glacial was reduced  
526 relative to today. We suggest that this reduction in the inflow of low-density SAMW during the LGM  
527 potentially had wider reaching implication for AMOC; the higher density of Atlantic AAIW relative to  
528 NADW may have contributed to a more sluggish overturning circulation in the Atlantic. In contrast,  
529 the subsequent southward migration of the SAF at 15-14 ka enabled a greater through-flow of low-  
530 density SAMW into the Atlantic, reducing the density of Atlantic AAIW and potentially contributing  
531 to the spin-up of AMOC during the Bølling-Allerød interstadial. If correct, our findings have  
532 significant implications for the importance of the Drake Passage in controlling AMOC stability.

533

### 534 **Acknowledgments**

535 We are grateful to S.J.Crowhurst, M.West and A.Hayton for providing technical assistance, and to  
536 M.Meredith for discussion. J.R. was funded jointly by the British Geological Survey/British Antarctic  
537 Survey (Natural Environment Research Council) and the University of Cambridge. ELM acknowledges  
538 funding from the Philip Leverhulme Prize. We thank the captain and crew of the RRS *James Clark*  
539 *Ross* for facilitating the collection of the marine sediment cores used in this study. The data reported  
540 in this paper are archived at [www.pangaea.de](http://www.pangaea.de)

541

542 **References**

- 543 Allison, L.C., Johnson, H.L., Marshall, D.P., Munday, D.R., 2010. Where do winds drive the Antarctic  
544 Circumpolar Current? *Geophys. Res. Lett.* 37, n/a-n/a. doi:10.1029/2010GL043355
- 545 Austin, J.J., Soubrier, J., Prevosti, F.J., Prates, L., Trejo, V., Mena, F., Cooper, A., 2013. The origins of  
546 the enigmatic Falkland Islands wolf. *Nat. Commun.* 4, 1552. doi:10.1038/ncomms2570
- 547 Barrows, T.T., Chen, M.-T., de Vernal, A., Eynaud, F., Hillaire-Marcel, C., Kiefer, T., Lee, K.E., Marret,  
548 F., Henry, M., Juggins, S., Londeix, L., Mangin, S., Matthiessen, J., Radi, T., Rochon, A., Solignac,  
549 S., Turon, J.-L., Waelbroeck, C., Weinelt, M., 2011. Various paleoclimate proxy parameters  
550 compiled within the MARGO project. doi:10.1594/PANGAEA.760904
- 551 Benthien, A., Müller, P.J., 2000. Anomalously low alkenone temperatures caused by lateral particle  
552 and sediment transport in the Malvinas Current region, western Argentine Basin. *Deep Sea Res.*  
553 *Part I* 47, 2369–2393. doi:10.1016/S0967-0637(00)00030-3
- 554 Bianchi, G.G., Hall, I.R., McCave, I.N., Joseph, L., 1999. Measurement of the sortable silt current  
555 speed proxy using the Sedigraph 5100 and Coulter Multisizer II: precision and accuracy.  
556 *Sedimentology* 46, 1001–1014. doi:10.1046/j.1365-3091.1999.00256.x
- 557 Blumberg, A.F., Mellor, G.L., 1987. A description of a Three-Dimensional Coastal Ocean Circulation  
558 Model, in: Heaps, N.S. (Ed.), *Three-Dimensional Coastal Ocean Models*, Coastal and Estuarine  
559 Sciences. American Geophysical Union, Washington, D. C., pp. 1–16. doi:10.1029/CO004
- 560 Brown, C.S., Newton, A.M.W., Huuse, M., Buckley, F., 2017. Iceberg scours, pits, and pockmarks in  
561 the North Falkland Basin. *Mar. Geol.* 386, 140–152. doi:10.1016/j.margeo.2017.03.001
- 562 Caniupán, M., Lamy, F., Lange, C.B., Kaiser, J., Arz, H., Kilian, R., Baeza Urrea, O., Arcena, C.,  
563 Hebbeln, D., Kissel, C., Laj, C., Mollenhauer, G., Tiedemann, R., 2011. Millennial-scale sea  
564 surface temperature and Patagonian Ice Sheet changes off southernmost Chile (53°S) over the  
565 past 60 kyr. *Paleoceanography* 26, PA3221. doi:10.1029/2010PA002049
- 566 Collins, L.G., Allen, C.S., Pike, J., Hodgson, D.A., Weckström, K., Massé, G., 2013. Evaluating highly  
567 branched isoprenoid (HBI) biomarkers as a novel Antarctic sea-ice proxy in deep ocean glacial  
568 age sediments. *Quat. Sci. Rev.* 79, 87–98. doi:10.1016/j.quascirev.2013.02.004
- 569 Combes, V., Matano, R.P., 2014. A two-way nested simulation of the oceanic circulation in the  
570 southwestern Atlantic. *J. Geophys. Res. Ocean.* 119, 731–756. doi:10.1002/2013JC009498
- 571 Conte, M.H., Sicre, M.-A., Röhlemann, C., Weber, J.C., Schulte, S., Schulz-Bull, D., Blanz, T., 2006.  
572 Global temperature calibration of the alkenone unsaturation index ( $U^{K^?}_{37}$ ) in surface waters  
573 and comparison with surface sediments. *Geochemistry, Geophys. Geosystems* 7, n/a-n/a.  
574 doi:10.1029/2005GC001054
- 575 Flügge, A., 1997. Variabilität von ungesättigten C 37 Methylketonen (Alkenone) in  
576 Sinkstoffallenmaterial der Norwegischen See und deren Abbildung in Oberflächensedimenten.  
577 Univ zu Kiel, Kiel Ph.D. Dissertation.
- 578 Gersonde, R., Crosta, X., Abelmann, A., Armand, L., 2005. Sea-surface temperature and sea ice  
579 distribution of the Southern Ocean at the EPILOG Last Glacial Maximum—a circum-Antarctic view  
580 based on siliceous microfossil records. *Quat. Sci. Rev.* 24, 869–896.  
581 doi:10.1016/j.quascirev.2004.07.015

582 Gordon, A.L., Weiss, R.F., Smethie, W.M., Warner, M.J., 1992. Thermocline and intermediate water  
583 communication between the south Atlantic and Indian oceans. *J. Geophys. Res.* 97, 7223.  
584 doi:10.1029/92JC00485

585 Hartin, C.A., Fine, R.A., Sloyan, B.M., Talley, L.D., Chereskin, T.K., Happell, J., 2011. Formation rates of  
586 Subantarctic mode water and Antarctic intermediate water within the South Pacific. *Deep Sea*  
587 *Res. Part I Oceanogr. Res. Pap.* 58, 524–534. doi:10.1016/j.dsr.2011.02.010

588 Ho, S.L., Mollenhauer, G., Lamy, F., Martínez-García, A., Mohtadi, M., Gersonde, R., Hebbeln, D.,  
589 Nunez-Ricardo, S., Rosell-Melé, A., Tiedemann, R., 2012. Sea surface temperature variability in  
590 the Pacific sector of the Southern Ocean over the past 700 kyr. *Paleoceanography* 27, n/a-n/a.  
591 doi:10.1029/2012PA002317

592 Hogg, A.M.C., Meredith, M.P., Blundell, J.R., Wilson, C., Hogg, A.M.C., Meredith, M.P., Blundell, J.R.,  
593 Wilson, C., 2008. Eddy Heat Flux in the Southern Ocean: Response to Variable Wind Forcing. *J.*  
594 *Clim.* 21, 608–620. doi:10.1175/2007JCLI1925.1

595 Howe, J.N.W., Piotrowski, A.M., Oppo, D.W., Huang, K.-F., Mulitza, S., Chiessi, C.M., Blusztajn, J.,  
596 2016. Antarctic intermediate water circulation in the South Atlantic over the past 25,000?years.  
597 *Paleoceanography* 31, 1302–1314. doi:10.1002/2016PA002975

598 Kaiser, J., Lamy, F., Hebbeln, D., 2005. A 70-kyr sea surface temperature record off southern Chile  
599 (Ocean Drilling Program Site 1233). *Paleoceanography* 20, n/a-n/a. doi:10.1029/2005PA001146

600 Keeling, R.F., Stephens, B.B., 2001. Antarctic sea ice and the control of Pleistocene climate instability.  
601 *Paleoceanography* 16, 112–131. doi:10.1029/2000PA000529

602 Koenitz, D., White, N., McCave, I.N., Hobbs, R., 2008. Internal structure of a contourite drift  
603 generated by the Antarctic Circumpolar Current. *Geochemistry, Geophys. Geosystems* 9, n/a-  
604 n/a. doi:10.1029/2007GC001799

605 Könitzer, S.F., Leng, M.J., Davies, S.J., Stephenson, M.H., 2012. An assessment of geochemical  
606 preparation methods prior to organic carbon concentration and carbon isotope ratio analyses  
607 of fine-grained sedimentary rocks. *Geochemistry, Geophys. Geosystems* 13.  
608 doi:10.1029/2012GC004094

609 Kornilova, O., Rosell-Melé, A., 2003. Application of microwave-assisted extraction to the analysis of  
610 biomarker climate proxies in marine sediments. *Org. Geochem.* 34, 1517–1523.  
611 doi:10.1016/S0146-6380(03)00155-4

612 Lambert, F., Delmonte, B., Petit, J.R., Bigler, M., Kaufmann, P.R., Hutterli, M.A., Stocker, T.F., Ruth,  
613 U., Steffensen, J.P., Maggi, V., 2008. Dust-climate couplings over the past 800,000 years from  
614 the EPICA Dome C ice core. *Nature* 452, 616–619. doi:10.1038/nature06763

615 Lamy, F., Arz, H.W., Kilian, R., Lange, C.B., Lembke-Jene, L., Wengler, M., Kaiser, J., Baeza-Urrea, O.,  
616 Hall, I.R., Harada, N., Tiedemann, R., 2015. Glacial reduction and millennial-scale variations in  
617 Drake Passage throughflow. *Proc. Natl. Acad. Sci. U. S. A.* 112, 13496–501.  
618 doi:10.1073/pnas.1509203112

619 Lamy, F., Kilian, R., Arz, H.W., Francois, J.-P., Kaiser, J., Prange, M., Steinke, T., 2010. Holocene  
620 changes in the position and intensity of the southern westerly wind belt. *Nat. Geosci.* 3, 695–  
621 699. doi:10.1038/ngeo959

- 622 McCave, I.N., Crowhurst, S.J., Kuhn, G., Hillenbrand, C.-D., Meredith, M.P., 2014. Minimal change in  
623 Antarctic Circumpolar Current flow speed between the last glacial and Holocene. *Nat. Geosci.* 7,  
624 113–116. doi:10.1038/ngeo2037
- 625 McCave, I.N., Manighetti, B., Robinson, S.G., 1995. Sortable silt and fine sediment size/composition  
626 slicing: Parameters for palaeocurrent speed and palaeoceanography. *Paleoceanography* 10,  
627 593–610. doi:10.1029/94PA03039
- 628 McClymont, E.L., Rosell-Melé, A., Giraudeau, J., Pierre, C., Lloyd, J.M., 2005. Alkenone and coccolith  
629 records of the mid-Pleistocene in the south-east Atlantic: Implications for the UK'37 index and  
630 South African climate. *Quat. Sci. Rev.* 24, 1559–1572. doi:10.1016/j.quascirev.2004.06.024
- 631 McManus, J.F., Francois, R., Gherardi, J.-M., Keigwin, L.D., Brown-Leger, S., 2004. Collapse and rapid  
632 resumption of Atlantic meridional circulation linked to deglacial climate changes. *Nature* 428,  
633 834–837. doi:10.1038/nature02494
- 634 Moffa-Sanchez, P., Hall, I.R., Thornalley, D.J.R., Barker, S., Stewart, C., 2015. Changes in the strength  
635 of the Nordic Seas Overflows over the past 3000 years. *Quat. Sci. Rev.* 123, 134–143.  
636 doi:10.1016/j.quascirev.2015.06.007
- 637 Nielsen, S.H.H., Koç, N., Crosta, X., 2004. Holocene climate in the Atlantic sector of the Southern  
638 Ocean: Controlled by insolation or oceanic circulation? *Geology* 32, 317. doi:10.1130/G20334.1
- 639 Orsi, A.H., Whitworth, T., Nowlin, W.D., 1995. On the meridional extent and fronts of the Antarctic  
640 Circumpolar Current. *Deep Sea Res. Part I* 42, 641–673. doi:10.1016/0967-0637(95)00021-W
- 641 Palma, E.D., Matano, R.P., Piola, A.R., 2008. A numerical study of the Southwestern Atlantic Shelf  
642 circulation: Stratified ocean response to local and offshore forcing. *J. Geophys. Res.* 113,  
643 C11010. doi:10.1029/2007JC004720
- 644 Peck, V.L., Hall, I.R., Zahn, R., Elderfield, H., 2008. Millennial-scale surface and subsurface  
645 paleothermometry from the northeast Atlantic, 55-8 ka BP. *Paleoceanography* 23, n/a-n/a.  
646 doi:10.1029/2008PA001631
- 647 Peterson, R.G., Stramma, L., 1991. Upper-level circulation in the South Atlantic Ocean. *Prog.*  
648 *Oceanogr.* 26, 1–73. doi:10.1016/0079-6611(91)90006-8
- 649 Poole, R., Tomczak, M., 1999. Optimum multiparameter analysis of the water mass structure in the  
650 Atlantic Ocean thermocline. *Deep Sea Res. Part I Oceanogr. Res. Pap.* 46, 1895–1921.  
651 doi:10.1016/S0967-0637(99)00025-4
- 652 Prah, F.G., Muehlhausen, L.A., Zahnle, D.L., 1988. Further evaluation of long-chain alkenones as  
653 indicators of paleoceanographic conditions. *Geochim. Cosmochim. Acta* 52, 2303–2310.  
654 doi:10.1016/0016-7037(88)90132-9
- 655 Renault, A., Provost, C., Sennéchaël, N., Barré, N., Kartavtseff, A., 2011. Two full-depth velocity  
656 sections in the Drake Passage in 2006-Transport estimates. *Deep Sea Res. Part II* 58, 2572–2591.  
657 doi:10.1016/j.dsr2.2011.01.004
- 658 Roberts, J., Gottschalk, J., Skinner, L.C., Peck, V.L., Kender, S., Elderfield, H., Waelbroeck, C., Vázquez  
659 Riveiros, N., Hodell, D.A., 2016. Evolution of South Atlantic density and chemical stratification  
660 across the last deglaciation. *Proc. Natl. Acad. Sci. U. S. A.* 113, 514–519.  
661 doi:10.1073/pnas.1511252113

- 662 Rosell-Mele, A., Carter, J.F., Parry, A.T., Eglinton, G., 1995. Determination of the UK'37 index in  
663 geological samples. *Anal. Chem.* 67, 1283–1289. doi:10.1021/ac00103a021
- 664 Rosell-Melé, A., Prah, F.G., 2013. Seasonality of UK'37 temperature estimates as inferred from  
665 sediment trap data. *Quat. Sci. Rev.* 72, 128–136. doi:10.1016/j.quascirev.2013.04.017
- 666 Santos, T.P., Lessa, D.O., Venancio, I.M., Chiessi, C.M., Mulitza, S., Kuhnert, H., Govin, A., Machado,  
667 T., Costa, K.B., Toledo, F., Dias, B.B., Albuquerque, A.L.S., 2017. Prolonged warming of the Brazil  
668 Current precedes deglaciations, *Earth and Planetary Science Letters*.  
669 doi:10.1016/j.epsl.2017.01.014
- 670 Skinner, L.C., Scrivner, A.E., Vance, D., Barker, S., Fallon, S., Waelbroeck, C., 2013. North Atlantic  
671 versus Southern Ocean contributions to a deglacial surge in deep ocean ventilation. *Geology* 41,  
672 667–670. doi:10.1130/G34133.1
- 673 Strub, P.T., Mesias, J.M., Montecino, V., Rutllant, J., Salinas, S., 1998. Coastal ocean circulation off  
674 western South America, in: Robinson, A.R., Brink, K.H. (Eds.), *The Global Coastal Ocean:  
675 Regional Studies and Syntheses*. Wiley, New York, pp. 273–314.
- 676 Stuart, K.M., Long, D.G., 2011. Tracking large tabular icebergs using the SeaWinds Ku-band  
677 microwave scatterometer. *Deep Sea Res. Part II Top. Stud. Oceanogr.* 58, 1285–1300.  
678 doi:10.1016/j.dsr2.2010.11.004
- 679 Talley, L.D., 1999. Some aspects of ocean heat transport by the shallow, intermediate and deep  
680 overturning Circulations, in: Clark, P.U., Webb, R.S., Keigwin, L.D. (Eds.), *Mechanisms of Global  
681 Climate Change at Millennial Time Scales*. American Geophysical Union, Washington, D. C., pp.  
682 1–22.
- 683 Ternois, Y., Kawamura, K., Ohkouchi, N., Keigwin, L., 2000. Alkenone sea surface temperature in the  
684 Okhotsk Sea for the last 15 kyr. *Geochem. J.* 34, 283–293. doi:10.2343/geochemj.34.283
- 685 Thompson, A.F., 2008. The atmospheric ocean: eddies and jets in the Antarctic Circumpolar Current.  
686 *Philos. Trans. A. Math. Phys. Eng. Sci.* 366, 4529–41. doi:10.1098/rsta.2008.0196
- 687 Veres, D., Bazin, L., Landais, A., Toyé Mahamadou Kele, H., Lemieux-Dudon, B., Parrenin, F.,  
688 Martinerie, P., Blayo, E., Blunier, T., Capron, E., Chappellaz, J., Rasmussen, S.O., Severi, M.,  
689 Svensson, A., Vinther, B., Wolff, E.W., 2013. The Antarctic ice core chronology (AICC2012): an  
690 optimized multi-parameter and multi-site dating approach for the last 120 thousand years.  
691 *Clim. Past* 9, 1733–1748. doi:10.5194/cp-9-1733-2013
- 692 Volkman, J.K., Barrerr, S.M., Blackburn, S.I., Sikes, E.L., 1995. Alkenones in *Gephyrocapsa oceanica*:  
693 Implications for studies of paleoclimate. *Geochim. Cosmochim. Acta* 59, 513–520.  
694 doi:10.1016/0016-7037(95)00325-T
- 695 Weaver, A.J., Saenko, O.A., Clark, P.U., Mitrovica, J.X., 2003. Meltwater pulse 1A from Antarctica as a  
696 trigger of the Bølling-Allerød warm interval. *Science* 299, 1709–13.  
697 doi:10.1126/science.1081002
- 698 Weber, M.E., Clark, P.U., Kuhn, G., Timmermann, A., Spreng, D., Gladstone, R., Zhang, X., Lohmann,  
699 G., Menviel, L., Chikamoto, M.O., Friedrich, T., Ohlwein, C., 2014. Millennial-scale variability in  
700 Antarctic ice-sheet discharge during the last deglaciation. *Nature* 510, 134–8.  
701 doi:10.1038/nature13397
- 702



703

704

## Supporting Material

705 Understanding the sortable silt flow speed proxy in marine systems with varying supply

706 The sortable silt proxy is predicated upon the premise that the grain-size of deposited sediment at a  
707 point is primarily controlled by the short term (a few tens of years) time history of flow speeds at that  
708 point acting on a broad spectrum of fine sediment sizes delivered along the transport path. Control of  
709 deposition is expressed in the classical Krone equation (Einstein and Krone, 1962; Krone, 1962) for the  
710 selective deposition of fine suspended material. The amount deposited is given by:

$$711 \quad \Sigma R_i t = \Sigma C_i w_{si} (1 - \tau_o / \tau_{di}) t$$

712 where  $R_i$  is the rate of deposition (dimensions mass/area.time;  $ML^{-2}T^{-1}$ ), thus  $\Sigma R_i t$  is ( $ML^{-2}$ ), to be  
713 summed over  $i$  size fractions. The controls are; settling velocity  $w_{si}$ , critical depositional stress  $\tau_{di}$ ,  
714 boundary shear stress  $\tau_o$  and the concentration  $C_i$  for each fraction according to the size distribution  
715 supplied in suspension from upstream.

716 This has been set out extensively in the publications of McCave, 2008, 2007; McCave et al., 1995;  
717 McCave and Hall, 2006. All the material that is considered in the analysis of the proxy is derived from  
718 terrestrial sources because care is taken to remove biogenic components (carbonate and silica) of  
719 marine origin. These sediments are delivered to the ocean beyond the shelf via a variety of routes,  
720 primarily by gravity flows (turbidity currents and debris flows) and shelf-edge resuspension/ spill-  
721 over, but also in a number of cases by aeolian fallout and via ice rafting in polar areas. Direct fluvial  
722 supply is rare, particularly at present under high sea-level stand. Even under glacially lowered sea-  
723 levels many deltas did not reach the shelf edge and many others debouched directly into the heads  
724 of submarine canyons, feeding turbidity currents which led into the deep sea (see reviews by e.g.  
725 McCave, 2002; Thomsen et al., 2002).

726 A test of whether sediments are current sorted or not is derived from cross-plots of  $\overline{SS}$  against  $SS\%$ .  
727 Under a current sorted regime,  $\overline{SS}$  correlates positively with  $SS\%$ , whereas unsorted sediments show  
728 no correlation. The latter case is evident in a fluvially-supplied lake (Gammon et al., 2017) or in the  
729 sediments from the Mississippi delta top (Xu et al., 2016) (Figure S5). In contrast, the marine  
730 sediment cores in the Drake Passage in Lamy et al., (2015) show a high degree of sediment sorting  
731 (Lamy et al., (2015), their Figure S3). Similarly, GC528 (presented in this study) shows a strong  
732 correlation between  $\overline{SS}$  and  $SS\%$  (Figure S2a) suggesting that the sediment has been current sorted.  
733 Furthermore, even though there are high IRD concentrations in some intervals, there is no

734 correlation between IRD concentration and  $\overline{SS}$  (Figure S2b) and the samples containing IRD do not  
735 deviate from the  $\overline{SS}$ -SS% trend (Figure S2a).

736

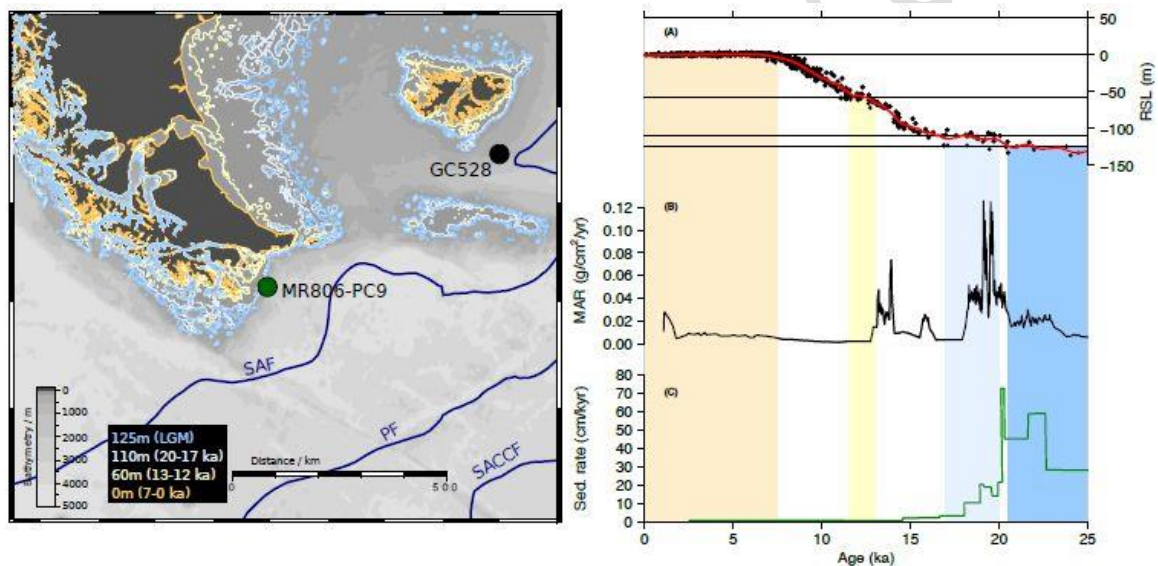
737

738

739

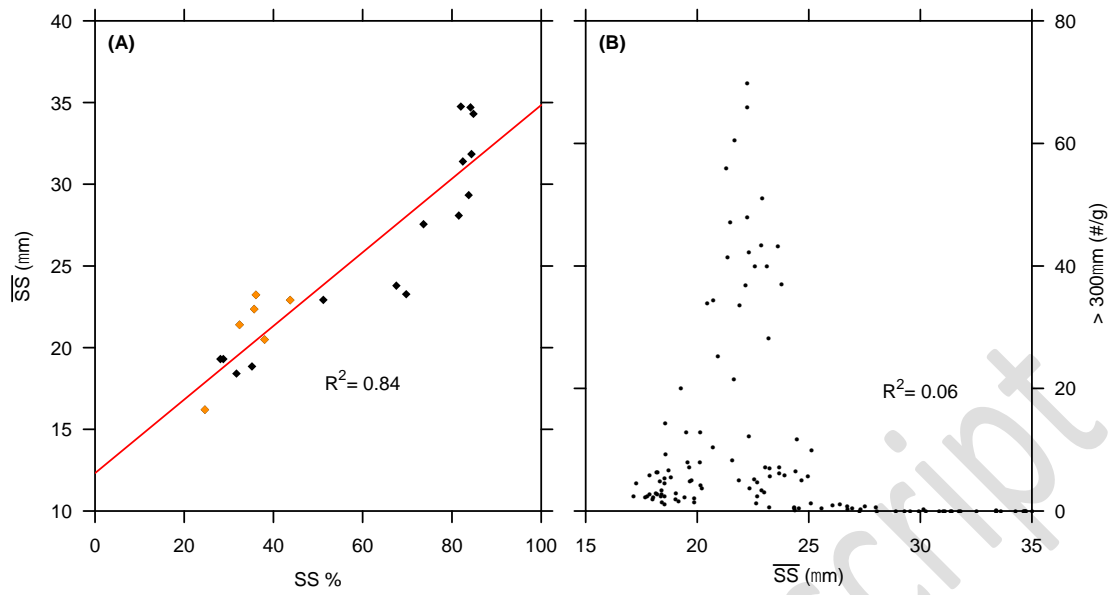
740

741 Supplementary Figures



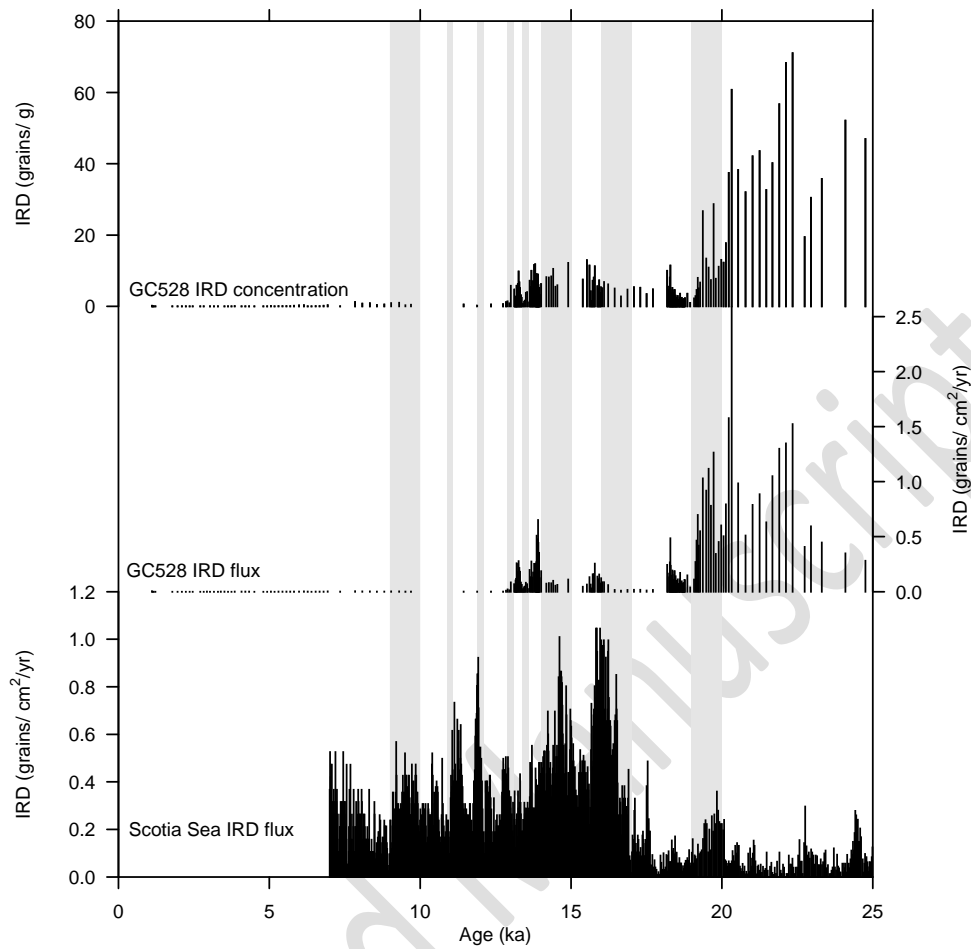
742

743 **Figure S1:** Assessing the impact of changes in sea level on the patterns of sedimentation. (Left) Map  
744 showing the position of the coastline at various intervals during the last deglaciation (see inset box)  
745 based on bathymetry. (Right) (A) Global relative sea level change over the last deglaciation (Lambeck  
746 et al., 2014); (B) Mass accumulation rate at site GC528; (C) Sedimentation rate at site MR806-PC9  
747 (Lamy et al., 2015).



748

749 **Figure S2:** Assessing the current sorting in core GC528. (A) Cross-plot of weight percentage sortable  
 750 silt fraction (10-63 $\mu\text{m}$ ) versus the mean sortable silt grain size. Samples that contain significant  
 751 quantities of IRD (grains > 300 $\mu\text{m}$ ) are shown in orange. (B) Cross-plot of mean sortable silt grain size  
 752 versus IRD (grains > 300 $\mu\text{m}$ ) concentration.



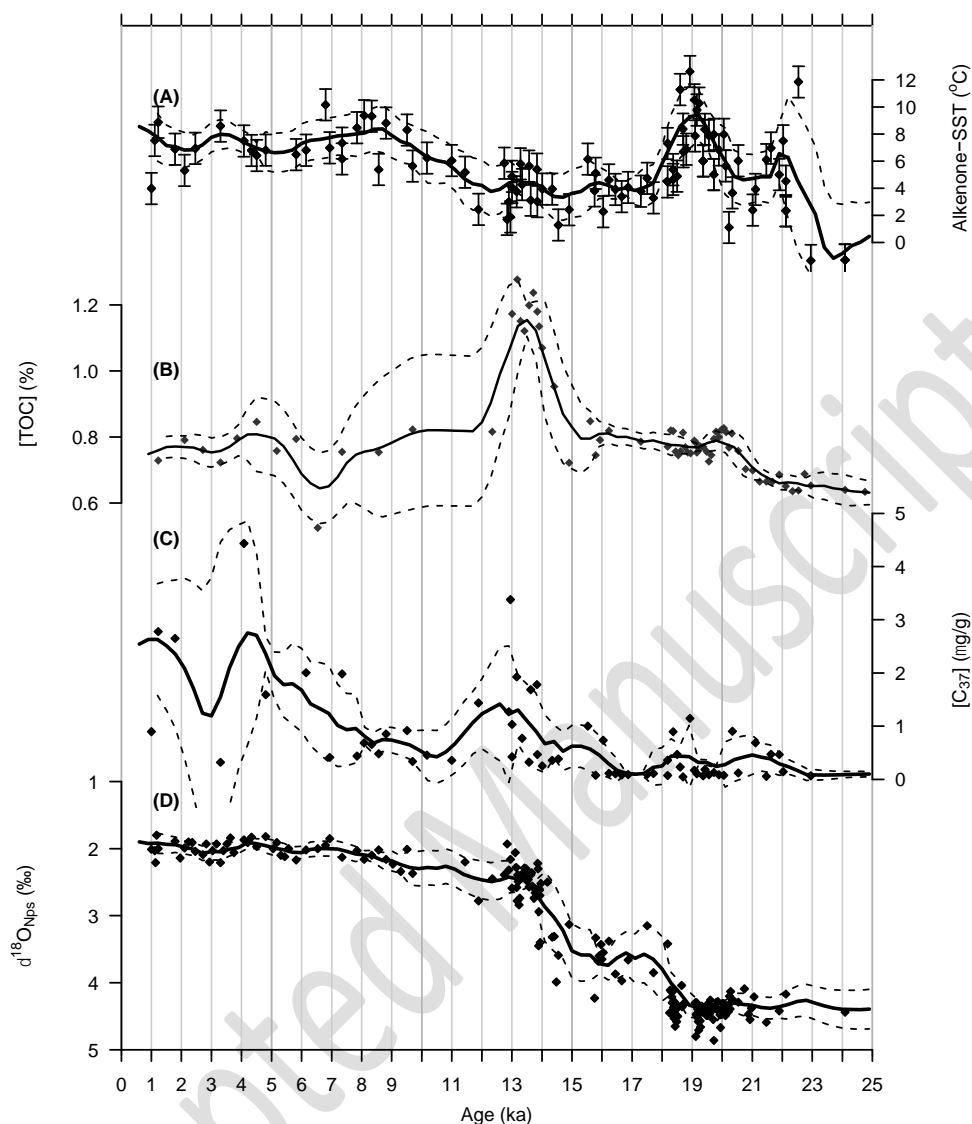
753

754 **Figure S3:** Comparison of the IRD records from the Southwest Atlantic (GC528) and the Scotia Sea

755 (Weber et al., 2014). (A) GC528 IRD concentration; (B) GC528 IRD flux (based on mass

756 accumulation rates); (C) Scotia Sea IRD flux. Grey bars show the Antarctic Icesheet Discharge

757 events (AIDS; Weber et al., 2014)

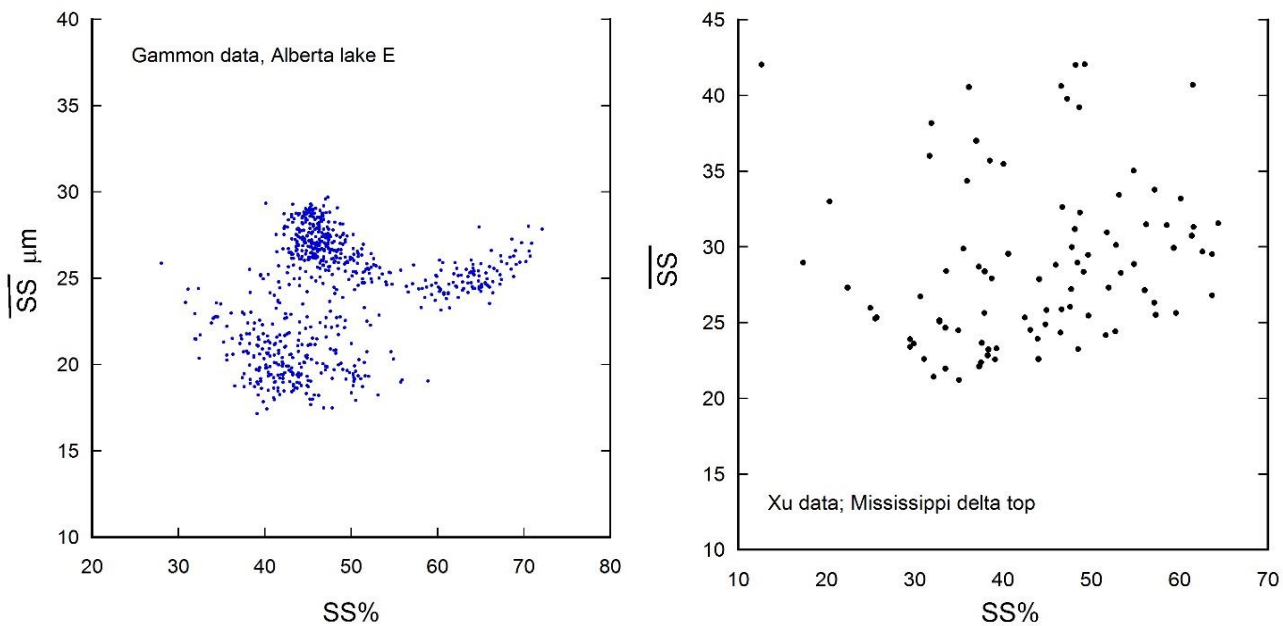


758

759 **Figure S4:** Assessing the potential for reworked alkenones having affected the LGM alkenone-SST  
 760 record. (A) Alkenone-derived SST records from downstream (GC528 - black) of the Drake Passage; (B)  
 761 Total organic carbon concentration in GC528; (C) Total alkenone concentration in GC528; (D)  
 762 Planktonic foraminifera *Neogloboquadrina pacherma (sinistral)*  $\delta^{18}\text{O}$  from GC528.

763

764



766 **Figure S5:** Unsorted sediment cross-plots from the fluvially dominated Alberta Lake (left; Gammon  
 767 et al., 2017) and the Mississippi delta top (right; Xu et al., 2016)

768

769

770 References

771 Einstein, H.A., Krone, R.B., 1962. Experiments to determine modes of cohesive sediment transport in  
 772 salt water. *J. Geophys. Res.* 67, 1451–1461.

773 Gammon, P.R., Neville, L.A., Patterson, R.T., Savard, M.M., Swindles, G.T., 2017. A log-normal  
 774 spectral analysis of inorganic grain-size distributions from a Canadian boreal lake core: Towards  
 775 refining depositional process proxy data from high latitude lakes. *Sedimentology* 64, 609–630.  
 776 doi:10.1111/sed.12281

777 Krone, R.B., 1962. Flume studies of the transport of sediment in estuarial shoaling processes, Final  
 778 Report, Hydraulic Engineering Laboratory and Sanitary Engineering Research Laboratory,  
 779 University of California.

780 Lambeck, K., Rouby, H., Purcell, A., Sun, Y., Sambridge, M., 2014. Sea level and global ice volumes  
 781 from the Last Glacial Maximum to the Holocene. *Proc. Natl. Acad. Sci. U. S. A.* 111, 15296–  
 782 15303. doi:10.1073/pnas.1411762111

783 Lamy, F., Arz, H.W., Kilian, R., Lange, C.B., Lembke-Jene, L., Wengler, M., Kaiser, J., Baeza-Urrea, O.,  
 784 Hall, I.R., Harada, N., Tiedemann, R., 2015. Glacial reduction and millennial-scale variations in  
 785 Drake Passage throughflow. *Proc. Natl. Acad. Sci. U. S. A.* 112, 13496–501.  
 786 doi:10.1073/pnas.1509203112

787 McCave, I.N., 2008. Size Sorting during transport and deposition of fine sediments. Sortable silt and  
 788 flow speed, in: Rebesco, M., Camerlenghi, A. (Eds.), *Developments in Sedimentology*. Elsevier,

789 Amsterdam, pp. 121–142. doi:10.1016/S0070-4571(08)10008-5

790 McCave, I.N., 2007. Deep-sea sediment deposits and properties controlled by currents, in: Hillaire-  
791 Marcel, C., de Vernal, A. (Eds.), *Proxies in Late Cenozoic Paleoceanography*. Elsevier,  
792 Amsterdam, pp. 19–62. doi:10.1016/S1572-5480(07)01006-8

793 McCave, I.N., 2002. Sedimentary settings on continental margins - an overview, in: Wefer, G., Billet,  
794 D., Hebbeln, D., Jorgensen, B.B., Schlüter, M., van Weering, T.C.E. (Eds.), *Ocean Margin  
795 Systems*. Springer Berlin Heidelberg, Berlin, Heidelberg, pp. 1–14. doi:10.1007/978-3-662-  
796 05127-6\_1

797 McCave, I.N., Hall, I.R., 2006. Size sorting in marine muds: Processes, pitfalls, and prospects for  
798 paleoflow-speed proxies. *Geochem., Geophys. Geosyst.* 7, 37pp. doi:10.1029/2006GC001284

799 McCave, I.N., Manighetti, B., Robinson, S.G., 1995. Sortable silt and fine sediment size/composition  
800 slicing: Parameters for palaeocurrent speed and palaeoceanography. *Paleoceanography* 10,  
801 593–610. doi:10.1029/94PA03039

802 Thomsen, L., Weering, T. van, Blondel, P., Lampitt, R., Lamy, F., McCave, N., McPhail, S., Mienert, J.,  
803 Neves, R., D'Ozouville, L., Ristow, D., Waldmann, C., Wollast, R., 2002. Margin building -  
804 regulating processes, in: Wefer, G., Billet, D., Hebbeln, D., Jorgensen, B.B., Schlüter, M., van  
805 Weering, T.C.E. (Eds.), *Ocean Margin Systems*. Springer, Berlin, Heidelberg, pp. 195–203.  
806 doi:10.1007/978-3-662-05127-6\_12

807 Weber, M.E., Clark, P.U., Kuhn, G., Timmermann, A., Spreng, D., Gladstone, R., Zhang, X., Lohmann,  
808 G., Menviel, L., Chikamoto, M.O., Friedrich, T., Ohlwein, C., 2014. Millennial-scale variability in  
809 Antarctic ice-sheet discharge during the last deglaciation. *Nature* 510, 134–8.  
810 doi:10.1038/nature13397

811 Xu, K., Bentley, S., Robichaux, P., Sha, X., Yang, H., 2016. Implications of Texture and Erodibility for  
812 Sediment Retention in Receiving Basins of Coastal Louisiana Diversions. *Water* 8, 26.  
813 doi:10.3390/w8010026

814